Advancing FRP Retrieval: Bridging Theory and Application

Weizhi Deng, Meng Zhou, Jun Wang, *Senior Member, IEEE*, Zhixin Xue, Zhendong Lu, Xi Chen, Huanxin Zhang, David A. Peterson, Edward J. Hyer, and Arlindo M. da Silva

***Abstract*— This study addresses two key uncertainties in the fire radiative power (FRP) retrieval, which is essential for improving global top-down fire emission inventories. First, it proposes a novel FRP retrieval method by combining the ∼4 and ∼8.6 μm channels based on Monte Carlo simulation, which is verified using the Visible Infrared Imaging Radiometer Suite (VIIRS). The inclusion of the ∼8.6 μm channel significantly improves the accuracy of FRP retrieval, especially for highly smoldering fires. Second, atmospheric correction is conducted using outputs from the state-of-the-art unified linearized vector radiative transfer model (UNL-VRTM). The importance of atmospheric correction is demonstrated through the single-channel (∼4 μm) FRP retrievals from the Moderate Resolution Imaging Spectroradiometer (MODIS) active fire (AF), VIIRS AF, and VIIRS second-generation fire light detection algorithm (FILDA-2) products. Post-correction results show effective mitigation of nighttime FRP angular dependency, achieved by considering the enhanced atmospheric attenuation due to longer path length off-nadir. However, a residual daytime FRP angular dependency remains, likely due to the angular dependency of the thresholds used for daytime fire detection. Additionally, an enhanced agreement is observed between the VIIRS FILDA-2 FRP retrievals from the Suomi National Polar-orbiting Partnership (NPP) and National Oceanic and Atmospheric Administration (NOAA)-20 satellites after correction. Lastly, a global FRP increase is noted across all three products, with VIIRS AF and VIIRS FILDA-2 showing more significant increases (65.8% and 62.5%, respectively) than MODIS AF (20.8%). These advancements in FRP retrievals may enhance the downstream fire emission products, which will benefit the air pollution modeling community.**

***Index Terms*— Atmospheric correction, combustion efficiency, fire emission, fire radiative power (FRP), Moderate Resolution Imaging Spectroradiometer (MODIS), modified combustion efficiency (MCE), Visible Infrared Imaging Radiometer Suite (VIIRS), wildfire.**

NOMENCLATURE

AF	Active fire.
ASTER	Advanced Spaceborne Thermal Emission and Reflection Radiometer.
BOA	Bottom of atmosphere.
BT	Brightness temperature.
CMG	Climate modeling grid.
DNB	Day night band.
FILDA-2	Second-generation fire light detection algorithm.
FRP	Fire radiative power.
GEOS-FP	Goddard Earth Observing System forward processing.
I-Band	Imagery resolution band.
MAD	Mean absolute deviation.
M-Band	Moderate resolution band.
MCE	Modified combustion efficiency.
MODIS	Moderate Resolution Imaging Spectroradiometer.
MIR	Mid infrared.
NIR	Near infrared.
PDF	Probability density function.
PW	Precipitable water.
RSR	Relative spectral response.
TIR	Thermal infrared.
TOA	Top of atmosphere.
UNL-VRTM	Unified linearized vector radiative transfer model.
VEF	Visible energy fraction.
VIIRS	Visible Infrared Imaging Radiometer Suite.
VZA	Viewing zenith angle.

I. INTRODUCTION

TOP-DOWN approach and bottom-up methods [1] have been developed by previous studies for quantifying fire emissions that are known to have significant impacts on climate and human health [2], [3], [4], [5]. The top-down approach is based on FRP, which quantifies the rate of energy

Received 8 June 2024; revised 8 August 2024; accepted 20 September 2024. Date of publication 30 September 2024; date of current version 31 October 2024. This work was supported in part by the NASA's Terra, Aqua, and SNPP Program under Award 80NNSC21L1976; and in part by the NASA's Modeling and Analysis Program (MAP) under Award 80NSSC21K1494. *(Corresponding authors: Jun Wang; Meng Zhou.)*

Weizhi Deng, Jun Wang, Zhixin Xue, Xi Chen, and Huanxin Zhang are with the Department of Chemical and Biochemical Engineering and the Atmospheric and Environmental Research Laboratory, Iowa Technology Institute, The University of Iowa, Iowa City, IA 52242 USA (e-mail: weizhi-deng@uiowa.edu; jun-wang-1@uiowa.edu; zhixin-xue@uiowa.edu; xi-chen-4@uiowa.edu; huanxin-zhang@uiowa.edu).

Meng Zhou is with the Global Modeling and Assimilation Office, NASA Goddard Space Flight Center, Greenbelt, MD 20771 USA, and also with the Atmospheric and Environmental Research Laboratory, Iowa Technology Institute, The University of Iowa, Iowa City, IA 52242 USA (e-mail: mzhou16@umbc.edu).

Zhendong Lu is with the Interdisciplinary Graduate Program, Geo-Informatics and Atmospheric and Environmental Research Laboratory, Iowa Technology Institute, The University of Iowa, Iowa City, IA 52242 USA (e-mail: zhendong-lu@uiowa.edu).

David A. Peterson and Edward J. Hyer are with the Marine Meteorology Division, Naval Research Laboratory, Monterey, CA 93943 USA (e-mail: david.peterson@nrlmry.navy.mil; edward.hyer@nrlmry.navy.mil).

Arlindo M. da Silva is with the Global Modeling and Assimilation Office, NASA Goddard Space Flight Center, Greenbelt, MD 20771 USA (e-mail: arlindo.m.dasilva@nasa.gov).

This article has supplementary downloadable material available at https://doi.org/10.1109/TGRS.2024.3470538, provided by the authors.

Digital Object Identifier 10.1109/TGRS.2024.3470538

release in the form of radiation during pyrogenic reactions and is shown to be directly linked to the biomass combustion rate [6], [7], [8], [9]. In contrast, the bottom-up approach estimates the total biomass burned by a fire event with consideration of factors such as burned area, above-ground fuel loading, and combustion completeness, and further estimates the biomass combustion rate with assumptions or extra data describing the relative change of emission with time [10], [11], [12]. However, uncertainties in the bottom-up fuel loading assumptions remain substantial, ranging by a factor of 2–5 [13], [14]. The top-down approach offers the advantage of reduced uncertainties and greater consistency [15], [16], [17], [18]. Regardless of the approach used, the biomass combustion rate is multiplied by an emission factor to calculate the gas/aerosol emission rate [19]. Past development of fire emission inventories, coupled with chemical transport models, has significantly advanced the understanding of the factors driving fire occurrence, the magnitude and variability of fire emissions, as well as the air pollution impacts on the source and downwind regions [20], [21], [22], [23], [24], [25], [26], [27].

A foundational parameter needed by the top-down approach is FRP, which is often retrieved from satellites using the MIR channel. FRP values are included in fire products such as the MODIS AF product, the VIIRS AF product, and the Geostationary Operational Environmental Satellite (GOES)-R AF product [28], [29]. However, recent advancements in remote sensing techniques have expanded the characterization of fires beyond just FRP and have started to retrieve combustion efficiency by combining MIR, NIR, and visible spectra [30], [31], [32]. Measurements in the NIR and visible spectra are made available by the VIIRS day night band (DNB, $\sim$0.7 μm), which is sensitive to both natural light [33], [34] and artificial light [35], [36], [37] at night. This facilitated the development of the VIIRS FILDA-2 product, which provides retrievals of night-time visible energy fraction (VEF) and modified combustion efficiency (MCE) in addition to FRP to derive fire emission factors instantaneously for a given fire pixel [38].

Despite the mainstream use of FRP for fire emission estimates, retrievals of FRP are subject to two primary sources of uncertainty [39]. The FRP calculation is currently based exclusively on MIR ($\sim$4 μm) radiance without atmospheric correction in the above-mentioned AF/FRP products. The first source of uncertainty stems from using only the MIR radiance to approximate FRP in a linear fashion without an offset term (that is, only the slope is optimized, and the intercept is fixed as 0). This leads to an overall underestimation of FRP, especially for fires that are highly smoldering (by 20%) [9]. There have been studies using TIR ($\sim$11 μm) in addition to MIR to resolve fire temperature and fire area, such as via the bispectral Dozier method [40], based on which FRP can be calculated using the Stefan–Boltzmann's law [41]. However, the use of Dozier's method requires an estimation of background temperature, which the TIR channel is highly sensitive to [42]. Consequently, this approach may have large uncertainties in conditions where background pixels exhibit high temperature variability (i.e., large uncertainties in the background temperature estimate by averaging the background pixels) [39], [43], [44]. Although attempts have been made to retrieve FRP by simultaneously using three TIR channels, the retrieval accuracy is limited by the lack of MIR channels on ASTER [45]. To date, few studies have used multiple channels other than MIR and TIR to further mitigate the nonlinearity effects in the retrieval of FRP.

The second source of FRP uncertainty arises from the assumption that the MIR channel is free of atmospheric absorption [46]. In reality, the TOA radiance at MIR is attenuated by over 10% due to absorption predominantly from N_2, CO_2, and N_2O, as shown in Fig. 1(a). Water vapor, while less absorbing in this channel, exhibits high variability in terms of total loading and vertical distribution [47] and further introduces uncertainties in the TOA radiance, where the BT can differ by 5 K between dry and wet conditions [44]. Effectively, the absence of atmospheric correction has led to two artifacts. One is the angular dependency of FRP retrieval, with average FRP values (in units of MW·m^{-2}) about 50% smaller off-nadir compared to nadir [38]. This is because, for the same atmospheric condition, its air mass factor in the satellite measurements is larger and leads to more pronounced absorption (and attenuation) in the path length of radiative transfer when viewing zenith angle (VZA) increases off-nadir. This artifact in FRP retrieval significantly contributes to the angular dependency of subsequent top-down fire emission products [1], [48]. The other artifact is the discrepancies of FRP retrieved via different sensors. A 20% difference was found between the FRP retrievals in the MODIS AF and VIIRS AF products on a global scale [49]. This is largely due to both the sensor detection ability difference, and differences in the central wavelength and relative spectral response (RSR) function of their MIR channels, which in turn convolve with gas absorption spectra, translating to the differences in total absorption. Even for the same sensor (i.e., VIIRS) onboard different satellites (i.e., Suomi-NPP and NOAA-20), discrepancies can arise due to differences in their viewing geometry at the time of observation, and therefore differences in atmospheric absorption at the MIR channel [38].

To address the aforementioned two critical sources of FRP uncertainty, a method is developed to retrieve FRP using a combination of the VIIRS 4.05-μm channel (MIR) and 8.55-μm channel (referred to as TIR-short herein to differentiate from the $\sim$11-μm channel), which is more accurate than using MIR alone, as will be demonstrated with theoretical simulations. Second, atmospheric correction is conducted at these channels, which can be used to mitigate artifacts of FRP dependency on viewing geometry and reconcile discrepancies among the FRP retrievals in the MODIS AF, VIIRS AF, and VIIRS FILDA-2 products.

II. Previous Work on FRP Retrieval: Techniques and Limitations

The FRP in a pixel is defined as

$$\mathrm{FRP}_{\mathrm{true}} = A_{\mathrm{P}}\varepsilon\sigma\sum_{i=1}^{n} f_i T_i^4 \times 10^{-6} \tag{1}$$

where $\mathrm{FRP}_{\mathrm{true}}$ is the true radiative energy from all fire components within the pixel (MW), A_{P} is the pixel area (m^2), ε is the fire emissivity (usually assumed to be 1), σ is the Stefan–Boltzmann's constant (W·m^{-2}·K^{-4}), n is the number

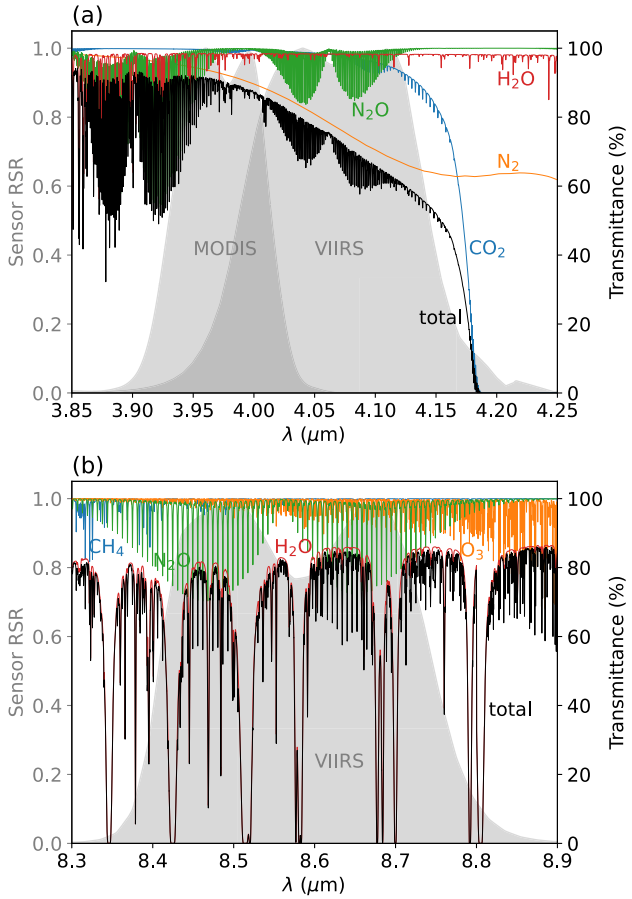

Fig. 1. Major gas absorption bands at (a) the MODIS MIR (channel 22, 3.96 μm) and VIIRS MIR (M13, 4.05 μm) channels and (b) the VIIRS TIR-short (M14, 8.55 μm) channel. The solid lines indicate the transmittance attributed to the individual gas component (or total gases), and the gray shaded area is the sensor RSR function.

of fire component in the pixel, f_i is the fraction (ratio of fire area to pixel area) of the ith fire component, T_i is the kinetic temperature (K) of the ith fire component, and 10^{-6} is the unit conversion factor from W to MW.

In reality, however, with only one or two channels for fire detection, we cannot resolve in a pixel the kinetic temperature and fraction of each individual fire (defined as a fire area with homogeneous temperature). Hence, assumptions and approximations have to be made for FRP calculation. In the original method for FRP calculation, Kaufman et al. [46] conducted a Monte Carlo simulation, where each fire pixel was composed of a randomized fraction of flaming fires, smoldering fires, and non-fire background. Subsequently, the true FRP within the fire pixel and the BOA 4-μm BT of the fire pixel and the background were fit with an empirical formula, which leads to the following 4-μm-BT-based estimate of FRP:

$$\mathrm{FRP_{BT}} = C\left(\mathrm{BT}^8_{4,\mathrm{BOA}} - \mathrm{BT}^8_{4\mathrm{b},\mathrm{BOA}}\right) A_\mathrm{P} \times 10^{-6} \qquad (2)$$

where $\mathrm{FRP_{BT}}$ (MW) is the FRP retrieved via the 4-μm-BT-based approach, the best-fit C is 4.34×10^{-19} W·m^{-2}·K^{-8}, $\mathrm{BT}_{4,\mathrm{BOA}}$ (K) is the BOA 4-μm BT of the fire pixel, and $\mathrm{BT}_{4\mathrm{b},\mathrm{BOA}}$ (K) is the background BOA 4-μm BT. Note that the best-fit C depends on the sensor RSR function and the set-up of Monte Carlo simulation. When using the VIIRS MIR RSR function and an improved Monte Carlo configuration based on VIIRS observation (see details in Section IV-A), the best-fit C is 4.20×10^{-19} W·m^{-2}·K^{-8} [Fig. 2(a)].

Going beyond the 4-μm-BT-based approach, Wooster et al. [39] proposed another approach for FRP calculation by directly using the 4-μm radiance. The step-by-step derivation of the 4-μm-radiance-based approach can be found in the Supplementary Material. Essentially, the true FRP can be fit by the 4-μm radiance in a linear manner

$$\mathrm{FRP_{rad}} = \frac{A_\mathrm{P}\sigma}{a}\left(L_{4,\mathrm{BOA}} - L_{4\mathrm{b},\mathrm{BOA}}\right) \times 10^{-6} \qquad (3)$$

where $\mathrm{FRP_{rad}}$ is the FRP (MW) retrieved using the 4-μm-radiance-based approach, $L_{4,\mathrm{BOA}}$ (W·m^{-2}·sr^{-1}·μm^{-1}) is the BOA upward 4-μm radiance of the fire pixel, $L_{4\mathrm{b},\mathrm{BOA}}$ (W·m^{-2}·sr^{-1}·μm^{-1}·K^{-4}) is the background BOA upward 4-μm radiance, and the best-fit parameter a is 2.90×10^{-9} (W·m^{-2}·sr^{-1}·μm^{-1}·K^{-4}). Again, the best-fit parameter a depends on the sensor RSR function and the Monte Carlo set-up. If the 4-μm radiance is convolved with sensor RSR function, a is 3.00×10^{-9} for MODIS (for both Terra and Aqua) and 2.88×10^{-9} for VIIRS (for both Suomi-NPP and NOAA-20). Note, in Wooster et al. [39], the derivation assumed a single fire component (with homogeneous fire temperature) within a fire pixel. Furthermore, only fire temperature was varied, and fire fractions were kept as constants in their empirical fitting to generate (3). A Monte Carlo simulation with a more accurate configuration was used considering multiple fire components and the variation of fire fraction (detailed in Section IV-A), and the best-fit a was found to be 3.01×10^{-9} for VIIRS (for both Suomi-NPP and NOAA-20) [Fig. 2(b)].

The advantage of using the 4-μm radiance is the simplicity in its linear approximation of FRP, whereas the 4-μm BT is a result of nonlinear transformation of radiance using the Planck function. Indeed, the hemispheric radiative power at a given wavelength for a fire is linearly proportional to radiance (with a constant factor of π) for that wavelength under the assumption that radiance is isotropic, while the BT has a more complex relationship with FRP that makes the empirical fitting between BT and FRP have larger uncertainties. This can be clearly seen in Fig. 2, where the 4-μm-BT-estimated FRP exhibits significant uncertainty (up to an order of magnitude) for a wide range of fire fraction, whereas the 4-μm-radiance-estimated FRP shows much less sensitivity. As a result, the radiance approach is overall superior with a 3% increase in R^2 (from 0.964 to 0.992), a 53.5% reduction in root mean square error (RMSE) (from 2.75 to 1.28 MW), and a 12.5% reduction in negative mean bias (from −0.24 to −0.21 MW). Note that the mean bias of the BT-based approach would be +0.04 MW if the coefficient from Kaufman et al. [46] is used (i.e., using $C = 4.34 \times 10^{-19}$ instead of $C = 4.20 \times 10^{-19}$ W·m^{-2}·K^{-8}). This explains that, after replacing the 4-μm-BT-based approach with the 4-μm-radiance-based approach in the MODIS AF product since collection 6, the global average FRP decreases by 16% [28]. Furthermore, for the same fire kinetic temperature and fire area, the 4-μm-BT-based approach provides inconsistent FRP retrieval off-nadir (VZA = 60°) compared with in-nadir as pixel size increases and fire fraction decreases, with a difference ranging from

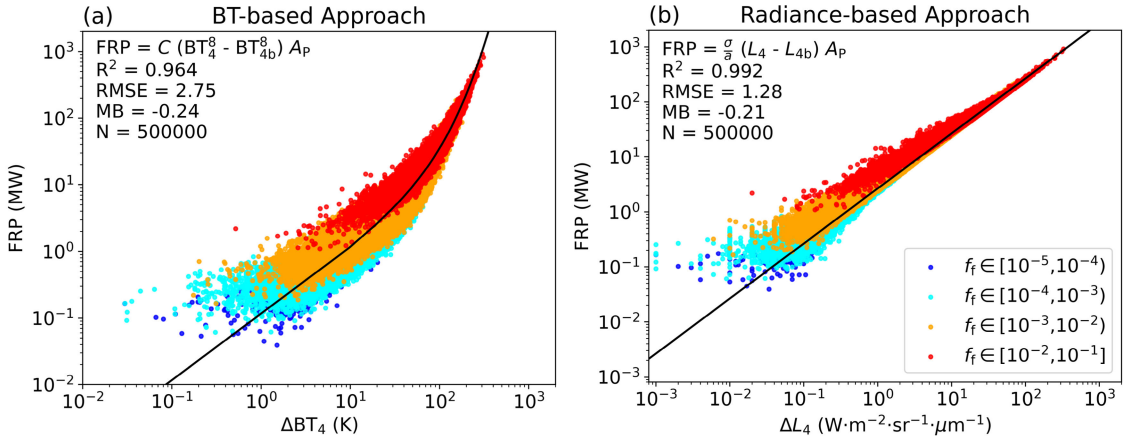

Fig. 2. (a) True FRP as a function of the 4-μm BT elevation from fires, with each dot representing a fire simulation from the Monte Carlo experiment, the color indicating fire fraction, and the black solid line indicating the best fit using the eighth power of 4-μm BT of the fire pixel and the background. (b) Similar to (a), the true FRP is plotted as a function of the 4-μm radiance elevation from fires. The black solid line indicates the best fit using the 4-μm radiance of the fire pixel and the background. Note that the axes are in log scale.

-5% to 20% (Fig. S1). This is largely due to the errors associated with the fitting of BT-FRP relationship with just one equation. Note that this FRP inconsistency of the 4-μm-BT-based approach even does not account for atmospheric pathlength difference (or atmospheric correction). In contrast, the 4-μm-radiance-based approach, because of a more accurate fitting, provides consistent FRP retrieval off-nadir and in-nadir, with negligible relative differences less than 10^{-9}. This consistency, however, is generated under the assumption that the radiance at BOA is known. The 4-μm-radiance-based approach is now widely used in fire products including VIIRS AF, GOES-R AF, and VIIRS FILDA-2 [29], [38].

While the 4-μm-radiance-based approach is widely used, it is important to recognize its uncertainty due to its assumption of a fixed linear relationship between FRP and 4-μm radiance regardless of fire temperature, as well as its omission of atmospheric correction. First, by assuming a fixed linear relationship between FRP and 4-μm radiance without an offset term, it leads to a significant underestimation of FRP (up to 20% and 40%, respectively) for smoldering fires and gas flares [9], [50]. Second, in the actual satellite retrieval, the measured TOA upward radiance should be first converted to BOA upward radiance before FRP calculation

$$\mathrm{FRP}_{\mathrm{rad}} = \frac{A_P(\theta)\sigma}{a(\Phi_4)\epsilon_4(\theta, p, \mathrm{PW}, \Phi_4)}(L_{4,\mathrm{TOA}} - L_{4b,\mathrm{TOA}}) \times 10^{-6} \quad (4)$$

where $L_{4,\mathrm{TOA}}$ and $L_{4b,\mathrm{TOA}}$ are now the measured TOA upward 4-μm radiance (W·m^{-2}·sr^{-1}·μm^{-1}) of the fire pixel and the background, and $\epsilon_4(\theta, p, \mathrm{PW}, \Phi_4)$ is the 4-μm atmospheric transmittance, which is needed to convert radiance from TOA to BOA. The transmittance is a function of the VZA (θ, unit: °), surface pressure (p, unit: hPa), and precipitable water (PW, unit: mm), which is further convolved with the sensor RSR function of the MIR channel (Φ_4). However, in the current MODIS and VIIRS AF/FRP products, the 4-μm atmospheric transmittance is assumed to be unity [28], [51]. This results in an angular dependency of FRP due to variations in the length of the light path and atmosphere transmittance at different VZAs (i.e., due to neglecting the ϵ_4 dependency on θ). For instance, Zhou et al. [38] showed that the FRP retrieval (in a unit of MW·m^{-2}) off-nadir on average is about 50% smaller than in nadir for VIIRS. The absence of atmospheric correction also entails the treatment of convolving gas absorption with the RSR function at the MIR channel, which is sensor-specific (i.e., ϵ_4 is a function of Φ_4). Li et al. [49] observed that VIIRS FRP density is roughly 20% higher than MODIS on global 1° × 1° grids from April 2016 to March 2017. However, when accounting for the effects of fire counts due to different sensor detection abilities, VIIRS average FRP density per fire count (in MW·m^{-2}·count^{-1}) is actually about 25% lower than MODIS. While no atmospheric correction is considered in Li et al. [49], the results highlight the need for treatment of atmospheric correction to reconcile different FRP products.

There have been studies to retrieve FRP based on fire kinetic temperature and fire area retrieved from the bispectral approach using channels at ~4 and ~11 μm [40], [41]

$$\mathrm{FRP}_{\mathrm{BS}} = A_P f_f \sigma \left(T_f^4 - T_b^4\right) \times 10^{-6} \quad (5)$$

where $\mathrm{FRP}_{\mathrm{BS}}$ (MW) is the FRP retrieved based on the bispectral approach, f_f and T_f are the effective fire fraction and effective fire kinetic temperature (K) retrieved via the bispectral approach, and T_b is the background kinetic temperature (K), which is usually assumed to be the background pixel mean TIR BT at BOA. The bispectral approach shows superior performance in theoretical simulations compared to one-channel approaches, with a negative mean bias within 10% (due to assuming a single fire in the pixel while there usually are multiple fire components) when the background temperature is known. However, this approach is highly sensitive to the estimates of 11-μm background BT, and a mere 1 K error in the 11-μm background BT estimate can contribute to an uncertainty exceeding 300% in the FRP retrieval [39]. In the actual satellite retrieval, the 11-μm background BT is usually approximated by averaging neighboring non-fire background pixels. The uncertainties of these estimates vary significantly, ranging from 0.5 K in eastern China to 4 K in boreal Canada and eastern United States [43]. Therefore, the accuracy of the bispectral approach is limited by the capability to accurately

represent the 11-μm background BT, with solely 7% of the fires whose FRP can be retrieved within reasonable accuracy from 2003 to 2012 using MODIS [43]. This limitation, however, could be mitigated by conducting atmospheric correction and considering point spread function to improve the fire and background BT estimates, and by removing low-confidence fires and clustering fire pixels to reduce the impacts from background BT estimation [42], [52]. The advantage of the bispectral approach is the simultaneous retrieval of fire kinetic temperature and fire area, based upon which FRP is calculated. This allows for the FRP flux (i.e., ratio of FRP to fire area) to be obtained, which is demonstrated to be a better indicator of how weather (such as wind speed and air temperature) affects fire dynamics than using FRP alone [44], [52].

It is noteworthy that efforts have been made to extract FRP from ASTER without the use of an MIR channel. Giglio et al. [45] fit the true FRP as a function of radiances from three TIR channels (i.e., 8.3, 9.1, and 11.3 μm) via a Monte Carlo simulation. However, limited by the lack of MIR channels on ASTER, this method can significantly underestimate FRP from flaming fires due to the low sensitivity of TIR to flaming temperature. Overall, it also performs less satisfactorily than the widely used 4-μm-radiance-based approach (Fig. S2). Therefore, the use of this approach is more suited to ASTER, where MIR channels are unavailable.

To summarize, there are four methods to retrieve FRP, namely the 4-μm-BT-based approach, the 4-μm-radiance-based approach, the bispectral approach, and the 3-TIR-radiance-based approach. The first two approaches both rely on a single channel (MIR), but the 4-μm-radiance approach is more accurate than the 4-μm-BT approach and is therefore popularly adopted by all operational algorithms for FRP retrieval. There exist at least two limitations in the 4-μm-radiance approach, which, respectively, arise from its linear approximation of FRP and the 4-μm radiance, and from its absence of atmospheric correction. While the bispectral approach employs two channels ($\sim$4 and $\sim$11 μm) to mitigate the nonlinearities in the FRP retrieval, the $\sim$11 μm channel is highly sensitive to background temperature, which can lead to high uncertainties when applied to actual satellite retrievals. The last approach is more suited to sensors such as ASTER, where MIR channels are unavailable.

This study explores the potential of two-channel FRP retrieval using channels other than $\sim$11 μm, along with $\sim$4 μm. It demonstrates that incorporating channels at shorter wavelengths where background signals are less significant (e.g., $\sim$8.6 μm) can improve the accuracy of FRP retrieval. Additionally, by fitting the true FRP with radiance from two channels, this study brings the same if not richer constraints than the bispectral approach for FRP estimate. This can simplify the retrieval process and avoid situations where there are no solutions for sub-pixel fire temperature and fire fraction (such as in cases where there are different types of fires within the same pixel).

III. Data

A. MODIS Active Fire Product

The level-2 MODIS Aqua AF product (MYD14) collection 6.1 spanning from June 2019 to May 2020 is employed in the study for one-channel (MIR) FRP atmospheric correction [28]. MODIS AF provides global FRP retrieval twice daily at a spatial resolution of 1 km. Only MODIS Aqua is used along with the VIIRS AF and VIIRS FILDA-2 products from the Suomi-NPP satellite, such that all products provide FRP retrievals at a satellite overpass time of 1:30 A.M./P.M. The product mainly uses the $\sim$4 μm channels (channels 21 and 22) and $\sim$11 μm channel (channel 31) for fire detection. The 4-μm radiance/BT is mainly derived from the low saturation channel 22 (saturating at 331 K) and is only derived from the high saturation channel 21 (saturating at 500 K) if the former saturates [53]. The 4-μm radiance is further used to calculate FRP using the radiance-based approach. Low-confidence fires are excluded from the analysis. The RSR function of the MODIS channel 22, which will be used for atmospheric correction, is shown in Fig. 1(a) and retrievable at https://mcst.gsfc.nasa.gov/calibration/parameters.

B. VIIRS Active Fire Product

The level-2 VIIRS 375 m AF product from Suomi-NPP (VNP14IMG) collection 2 (re-processed in January 2024) from June 2019 to May 2020 is used in the study for one-channel (MIR) FRP atmospheric correction [51], [54]. VIIRS AF provides global FRP retrieval twice daily at a spatial resolution of 375 m. It employs the high-resolution (375 m) I4 (3.74 μm) and I5 bands (11.45 μm) for fire detection. However, due to the low saturation of the single-gain I-bands, the product retrieves FRP using the radiance-based method based on the moderate-resolution (750 m) dual-gain M13 (4.05 μm) band. Specifically, the FRP is first determined based on the M-band pixel and then equally distributed to the collocated I-band fire pixels. During the study period, VIIRS AF products from Suomi-NPP and NOAA-20 are available, and only the product from Suomi-NPP is used in this study. Low-confidence fires are excluded from the analysis.

C. VIIRS FILDA-2 Product

The VIIRS FILDA-2 products obtained from Suomi-NPP and NOAA-20 are used in the study for one-channel (MIR) FRP atmospheric correction [38]. VIIRS FILDA-2 products offer global FRP retrieval twice daily with a spatial resolution of 375 m. VIIRS FILDA-2 from Suomi-NPP is primarily used in this study. Additionally, in Section V-C2, VIIRS FILDA-2 from NOAA-20 is compared with that from Suomi-NPP. Unless explicitly stated otherwise, the reference to the VIIRS FILDA-2 product in the article pertains to that obtained from Suomi-NPP.

Compared with the VIIRS AF product, VIIRS FILDA-2 incorporates the VIIRS DNB ($\sim$0.7 μm) in addition to the standard I bands to capture the visible and NIR signals from fires, leading to approximately 25%–30% more fires detected at night, especially those smaller and cooler fires that would otherwise be missed [38]. Furthermore, with the visible and NIR information added, VIIRS FILDA-2 not only offers FRP retrieval but also provides retrievals of nighttime VEF and MCE, which are indicators of the fire combustion phase and fire temperature [31]. The results generated from VIIRS FILDA-2 are available via

TABLE I
CONFIGURATION OF THE MONTE CARLO SIMULATION

	Component	Temperature (K)	Fraction
Fire pixel	Flaming Smoldering Background	$T_{\mathrm{fl}} \sim \mathrm{Normal}(1000, 100^2)$ $T_{\mathrm{sm}} \sim \mathrm{Normal}(600, 100^2)$ $T_{\mathrm{b}} \sim \mathrm{Normal}(300, 10^2)$	$\log_{10} f_{\mathrm{fl}} \sim \mathrm{Normal}(-3.5, 0.55^2)$ $\log_{10} f_{\mathrm{sm}} \sim \mathrm{Normal}(-3, 0.55^2)$ $f_{\mathrm{b}} = 1 - f_{\mathrm{fl}} - f_{\mathrm{sm}}$
Background pixel average	/	$\bar{T}_{\mathrm{bp}} \sim \mathrm{Normal}(T_{\mathrm{b}}, 1)$	/

http://esmc.uiowa.edu:3838/fires_detection. VIIRS FILDA-2 is currently being implemented by the National Aeronautics and Space Administration (NASA) and is anticipated to be publicly available by the end of 2024 at https://viirsland.gsfc.nasa.gov/Products/NASA/FILDA_ESDR.html.

Low-confidence fires are excluded from the analysis. Additionally, duplicate fires between scans, identified by a bow-tie-free fraction below 0.95, are discarded. Bow-tie-free fraction is defined for each fire detection as the ratio of the overlapping area between DNB (not affected by bow-tie effect) and I-band (affected by bow-tie effect), to the total I-band pixel area [30], [38]. A bow-tie-free fraction below 0.95 indicates that the fire detection is impacted by the bow-tie effect and is likely to be double- or even triple-counted. In addition, the RSR functions of the VIIRS M13 channel (4.05 μm) and M14 channel (8.55 μm) (shown in Fig. 1), which will be used in the atmospheric correction as well as in the two-channel FRP formula derivation, are retrieved from https://ncc.nesdis.noaa.gov/VIIRS/VIIRSSpectralResponseFunctions.php.

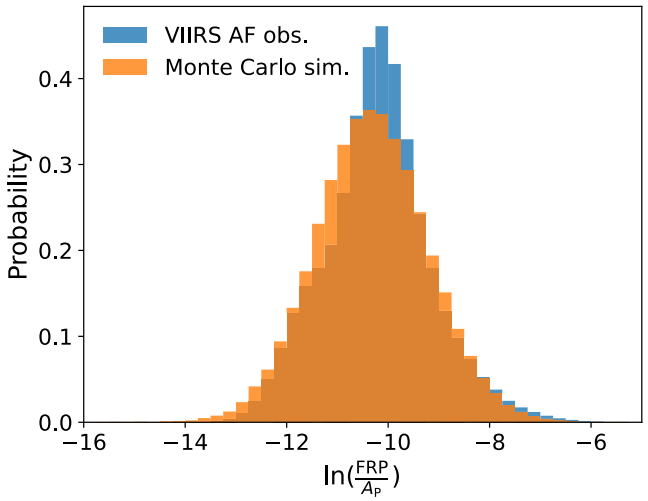

Fig. 3. PDFs of the natural logarithm of the FRP density (in MW·m^{-2}) for the Monte Carlo simulation (orange) and the actual VIIRS AF observation after atmospheric correction (blue). Note, to directly compare with observation, the FRP from the Monte Carlo simulation here is calculated based on the MIR radiance using (3).

D. Goddard Earth Observing System Forward Processing

To consider the variations of water vapor content in the atmospheric correction of FRP, the PW from the GEOS-FP is used during the one-year study period [55]. GEOS-FP provides weather and atmospheric composition forecasts by assimilating observations from various platforms. It provides the instantaneous total column PW vapor at a resolution of 0.25° × 0.3125° (latitude dimension × longitude dimension) every 3 h. In addition, surface pressure from GOES-FP is used for atmospheric correction, as it impacts the total amounts of gases in the path of radiative transfer, which further impacts total gas absorption and hence FRP retrieval. The forecast of PW and surface pressure will allow us to conduct FRP atmospheric correction not only in a reanalysis manner but also operationally for the VIIRS FILDA-2 product which is underway.

IV. TWO-CHANNEL FRP RETRIEVAL USING TIR-SHORT

A. Monte Carlo Simulation

To derive a formula for FRP retrieval using a combination of VIIRS MIR (4.05 μm) and TIR-short (8.55 μm) channels, Monte Carlo simulations are conducted to mimic the fire detection by satellite. For successful detection of fire pixels, it requires an estimate of the background MIR (~4 μm) and TIR (~11 μm) radiance, which is often characterized by averaging the radiance of non-fire background pixels. Therefore, simultaneous simulations of fire pixels and the corresponding background pixels are conducted. The design of the Monte Carlo simulation is shown in Table I.

Each simulated fire pixel consists of a randomized fraction of flaming fires, smoldering fires, and non-fire background. The flaming fraction is pseudo-randomly generated in a log-normal fashion, where the $\log_{10}$ of the flaming fraction obeys a Gaussian distribution with a mean of −3.5 and a standard deviation of 0.55. Similarly, the $\log_{10}$ of the smoldering fraction obeys a Gaussian distribution with a mean of −3 and a standard deviation of 0.55. The background fraction is then calculated based on the flaming and smoldering fraction. The temperature of each component is pseudo-randomly generated following a Gaussian distribution, with a mean of 1000 K and a standard deviation of 100 K for flaming fires, a mean of 600 K and a standard deviation of 100 K for smoldering fires, and a mean of 300 K and a standard deviation of 10 K for non-fire background [39]. The pixel size is set equal to that of the VIIRS I band in nadir (375 × 375 m), although this term ultimately cancels out and does not impact the derivation of the FRP formula.

The average temperature of the non-fire background pixels is pseudo-randomly generated following a Gaussian distribution. The mean is set equal to the temperature of the non-fire counterpart in the simulated fire pixel, and the standard deviation is set to 1 K. A standard deviation of 1 K is estimated based on the VIIRS FILDA-2 observations (see details in the Supplementary Material). Adding perturbation to the average temperature of background pixels is essential,

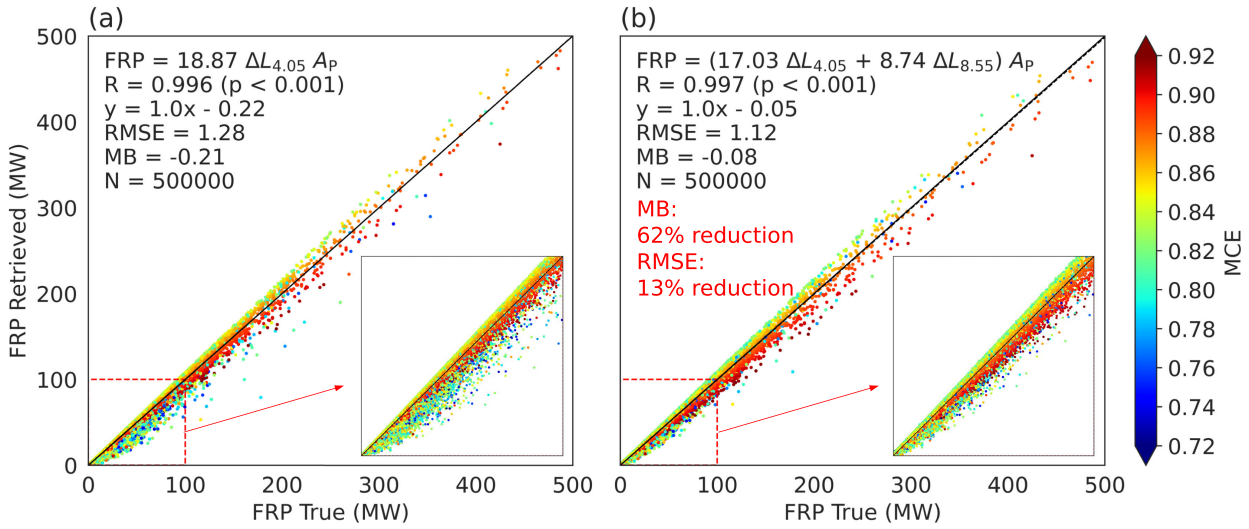

Fig. 4. Evaluation of (a) one-channel (MIR, 4.05 μm) FRP retrieval and (b) two-channel (MIR and TIR-short, 4.05 μm and 8.55 μm) FRP retrieval based on Monte Carlo simulation. Each dot indicates a fire simulation, with the color indicating the MCE. The black lines are the 1:1 line.

because, in reality, it can deviate from the true background temperature in the fire pixel. This is especially important at the TIR-short (8.55 μm) channel, as an uncertainty of 1 K in the background temperature in cases of small fires can lead to a ~50% difference in the TIR-short anomaly between the fire pixel and the background pixel average, thereby resulting in a ~6% difference in the two-channel FRP retrieval (for a typical small fire with a temperature of 800 K and a fraction of 10^{-3}).

For each fire simulation, the true FRP of the fire pixel is obtained using (1). The BOA upward radiance of the fire pixel and background pixel average is calculated using the Planck function assuming a blackbody behavior, which is further convolved with the sensor RSR function of the respective VIIRS channel. Then, the true FRP is fit as a function of the BOA upward radiance of the fire pixel and background pixel average by minimizing the least square errors.

In addition, the MCE of each fire simulation is approximated, as it is desirable to evaluate the FRP retrieving performance under different fire temperatures or fire combustion phases. It is approximated by the ratio of fire radiance at the visible channel to that at the MIR channel following Zhou et al. [38]:

$$\mathrm{MCE} = 1 + 0.017 \ln\left(\frac{\mathrm{VLP}}{\mathrm{FRP}}\right) \tag{6}$$

where MCE is the MCE of the simulated fire pixel, and VLP is the visible light power of the simulated fire pixel (approximated by its theoretical radiance at the VIIRS DNB).

Comparing the Monte Carlo simulation with the actual observation from the VIIRS AF product, their PDFs of the natural logarithm of the FRP density (in MW·m^{-2}) align closely (Fig. 3). Both PDFs exhibit a peak centered around −10.5, and their right tails extend to −6, highlighting the model capability in capturing the observed PDF of FRP. Notably, this set-up of the Monte Carlo simulation is an improvement upon the previous experiments [39], [46] in that it effectively represents the FRP distribution from the actual VIIRS observations.

B. Retrieval Evaluation

The true FRP within the fire pixel is empirically fit as a function of BOA upward radiance at the VIIRS MIR and TIR-short channels based on Monte Carlo simulation (Fig. 4). Building upon the 4 μm-radiance-based approach, we incorporate the TIR-short (8.55 μm) channel due to its high sensitivity to smoldering fires. The motives for including the TIR-short channel are that the majority of the fires from the Monte Carlo simulation are small and smoldering (Fig. 4). An experiment was conducted to retrieve FRP by incorporating the NIR (2.25-μm) channel, which would be more sensitive to flaming fires. However, no significant improvement was found in the overall performance (Fig. S3), as the output from the Monte Carlo simulation consists predominantly of smoldering fires. Note that only first-order terms are used in the fitting, as incorporating second- and third-order terms does not significantly improve the results.

The formula of the two-channel FRP retrieval is

$$\mathrm{FRP}_{2\mathrm{ch}} = A_{\mathrm{P}}\left[a_{4.05}\Delta L_{4.05,\mathrm{BOA}} + a_{8.55}\Delta L_{8.55,\mathrm{BOA}}\right] \times 10^{-6} \tag{7}$$

where $\mathrm{FRP}_{2\mathrm{ch}}$ (MW) is the retrieved FRP using two channels (i.e., MIR and TIR-short), A_{P} is pixel size (m^2), $\Delta L_{4.05,\mathrm{BOA}}$ and $\Delta L_{8.85,\mathrm{BOA}}$ (W·m^{-2}·sr^{-1}·μm^{-1}) are, respectively, the BOA upward MIR and TIR-short radiance anomaly between the fire pixel and background pixel average, the best-fit parameters $a_{4.05}$ and $a_{8.55}$ are, respectively, 17.03 and 8.74 (sr·μm), and 10^{-6} is the unit conversion factor from W to MW. As seen in Fig. 4, the two-channel retrieval outperforms the one-channel MIR retrieval, with an overall 62% reduction in negative mean bias (from −0.21 to −0.08 MW) and a 12.5% reduction in RMSE (from 1.28 to 1.12 MW). The improvement is more pronounced for smoldering fires (73% reduction in negative mean bias from −0.81 to −0.22 MW for fire with MCE < 0.8) owing to the enhanced sensitivity to smoldering temperature by introducing the TIR-short channel.

The two-channel FRP retrieval is further applied to the nighttime VIIRS FILDA-2 product. In situations where there

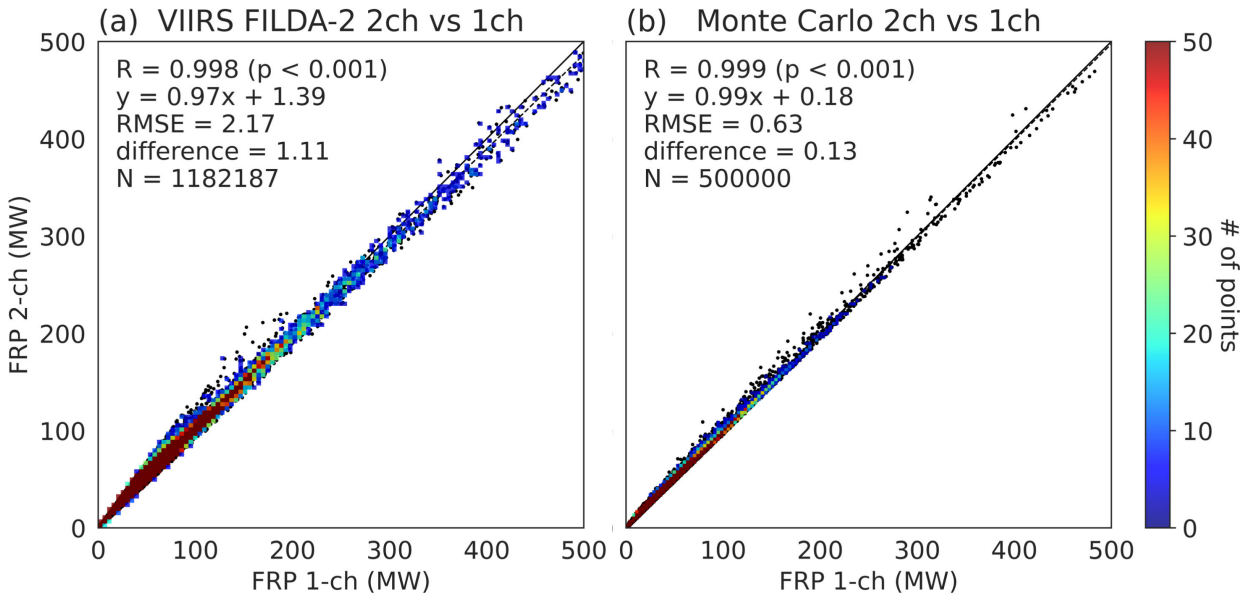

Fig. 5. Comparison between the two-channel and one-channel FRP retrieval of (a) nighttime VIIRS FILDA-2 product from June 2019 to May 2020 and (b) Monte Carlo simulation. The black solid line is the 1:1 line, the black dashed line is the best-fit line, and the color indicates the density of the data.

may be large uncertainties in discerning fire signals at the TIR-short channel, such as cases of negative TIR-short radiance anomaly or TIR-short radiance anomaly surpassing the MIR radiance anomaly, we resort to the one-channel FRP retrieval method. The comparison between the VIIRS FILDA-2 two-channel and one-channel FRP retrieval is shown in Fig. 5(a). Note that atmospheric correction at both channels (detailed in Section V) has been considered here. Overall, the comparison is consistent with the outcomes of the Monte Carlo simulation shown in Fig. 5(b). The one-channel and two-channel methods for VIIRS FILDA-2 exhibit a strong correlation of 0.998. The two-channel FRP retrieval has a positive mean difference of 1.11 MW compared to the one-channel method. This overall increase primarily stems from the increase in low FRP region (FRP $<$ 100 MW), which corresponds to the improvements for the predominantly smoldering fires in Fig. 4. In the high FRP region (FRP $>$ 300 MW), the two-channel retrieval tends to be slightly lower than the one-channel retrieval, consistent with Monte Carlo simulation. Note that this does not imply that the two-channel approach underestimates the true FRP, as it is in comparison to the one-channel method and not in reference to the true FRP. The two-channel retrieval results for Indonesia are depicted in Fig. 6(a). A significant FRP increase is found when employing the two-channel approach, especially for peat fires characterized by intense smoldering, as indicated by the low MCE values in Fig. 6(b). These results demonstrate the efficacy of the two-channel FRP retrieval method in the VIIRS FILDA-2 product, particularly in enhancing retrieval accuracy for highly smoldering fires.

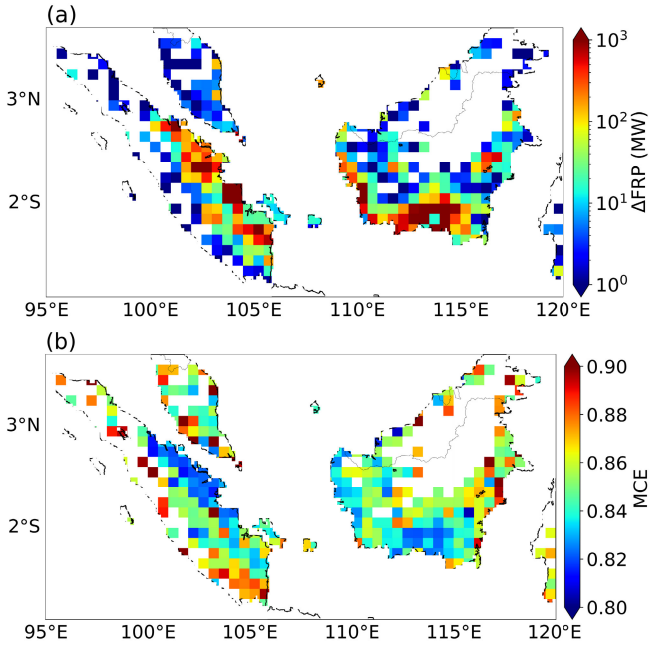

Fig. 6. (a) Difference between the two-channel and one-channel FRP retrieval and (b) MCE retrieval in Indonesia for the nighttime VIIRS FILDA-2 product from June 2019 to May 2020 (aggregated to 0.5° × 0.5° CMG).

C. Sensitivity Analysis

Uncertainties in the two-channel FRP retrieval can stem from several sources. These include: 1) uncertainties arising from approximating the nonlinear FRP using a linear combination of radiances from two channels (Fig. 4); 2) uncertainties associated with approximating the actual background radiance contribution with background pixel average; and 3) uncertainties in the estimation of the BOA fire pixel radiance.

To investigate the retrieval uncertainties due to the background radiance estimation, a sensitivity test is conducted assuming a 2 K standard deviation of the average background pixel temperature (as opposed to 1 K). For the two-channel FRP fitting, the RMSE increases by 8% when uncertainties in the background radiance estimation increase (Fig. S4).

The uncertainties in the BOA fire pixel radiance estimation are twofold: instrument noise at TOA and atmospheric correction to convert TOA radiance to BOA radiance. From the VIIRS Radiometric Calibration Algorithm Theoretical

Basis Document (ATBD) [56], the uncertainty in the TOA BT is approximately 0.7% and 0.4% for the MIR and TIR channels. Considering the noise in TOA BT leads to higher uncertainties in the two-channel fitting of FRP, with a 35% increase in RMSE and a 0.2% decrease in explained variability (Fig. S5). Nevertheless, it is still apparent that the two-channel retrieval outperforms the one-channel retrieval, demonstrating the robustness of the proposed two-channel retrieval method. Currently, the uncertainties and biases associated with the atmospheric correction are substantial, as no atmospheric correction is considered for the MODIS AF, VIIRS AF, and VIIRS FILDA-2 products. This will be illustrated in detail in Section V.

V. Atmospheric Correction

A. Radiative Transfer Modeling

In the actual satellite retrieval, atmospheric correction is required to convert the radiance from TOA to BOA before the FRP calculation. In this section, atmospheric correction is conducted on the MODIS and VIIRS MIR channels, which will be used for the one-channel FRP retrieval in the MODIS AF, VIIRS AF, and VIIRS FILDA-2 products. Additionally, atmospheric correction is conducted on the VIIRS TIR-short channel, which can be used for the potential two-channel FRP application on the VIIRS FILDA-2 product.

To simulate gas absorption and atmospheric transmittance for the atmospheric correction of FRP, the UNL-VRTM is employed [57], [58]. UNL-VRTM features VLIDORT as the core for radiative transfer, a linearized Mie-code and a T-matrix code for aerosol optical properties, a Rayleigh scattering module for molecular scattering, as well as a line-by-line gas absorption calculation using the HITRAN database. In the model, the one-way atmospheric transmittance is calculated as the ratio of the TOA to BOA upward radiance at various VZAs. This treatment is more accurate than a simplified approach where the optical depth is scaled by the cosine function at various VZAs, and the transmittance is calculated using Beer's law. This is because the mass of the atmosphere is not uniformly distributed along the light path, and nonlinearities can occur due to processes such as multiple scattering and coupling/interaction between the TOA light source (e.g., sunlight or moonlight), the surface, and the atmosphere. A sensitivity test shows that the difference in the VIIRS 4-μm transmittance between these two approaches is negligible in nadir but increases to 2.3% at VZA = 60° (Fig. S6). PW in the model is calculated using the following equation [59], [60]:

$$\mathrm{PW} = \frac{1}{\rho_{\mathrm{w}} g} \int_{p_{\mathrm{BOA}}}^{p_{\mathrm{TOA}}} x(p)\mathrm{d}p \tag{8}$$

where PW is the precipitable water (mm), ρ_{w} is the density of water (g·cm^{-3}), g is the acceleration due to gravity (m·s^{-2}), $x(p)$ is the average water vapor mixing ratio (kg·kg^{-1}) as a function of pressure (p, hPa), and p_{BOA} and p_{TOA} are, respectively, the pressure (hPa) at BOA and TOA.

Currently, only first-order atmospheric correction (i.e., due to gas absorption from the standard atmosphere) is considered. Second-order correction (i.e., due to absorption and scattering from the gaseous and aerosol emissions from fires) is not considered, as fire emissions are uncertain and constrained by FRP itself. Furthermore, upon conducting a Mie code calculation, the mass extinction efficiency of typical smoke particles decreases by over 90% from mid-visible to MIR, suggesting that smoke optical depth at ~4 μm is negligible. The results shown later in Section V-C1 will demonstrate that first-order atmospheric correction is sufficient to effectively

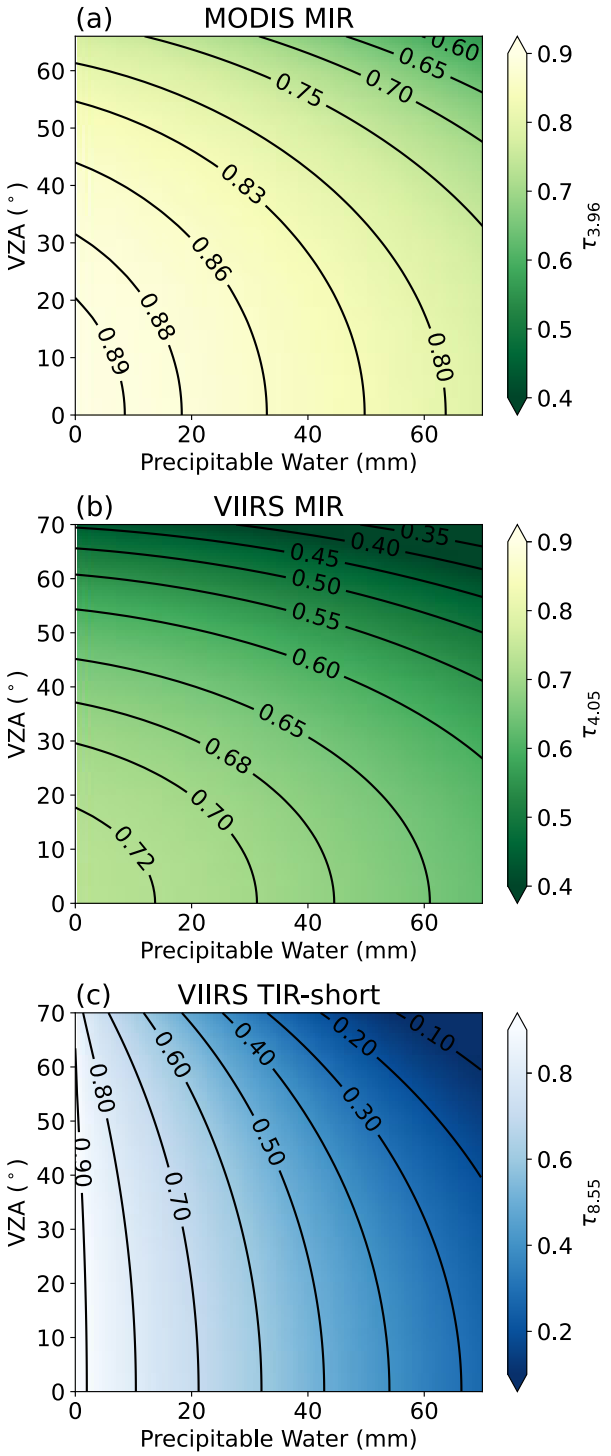

Fig. 7. Atmospheric transmittance as a function of VZA and PW at (a) the MODIS MIR channel (channel 22, 3.96 μm), (b) the VIIRS MIR channel (M13, 4.05 μm), and (c) the VIIRS TIR-short channel (M14, 8.55 μm).

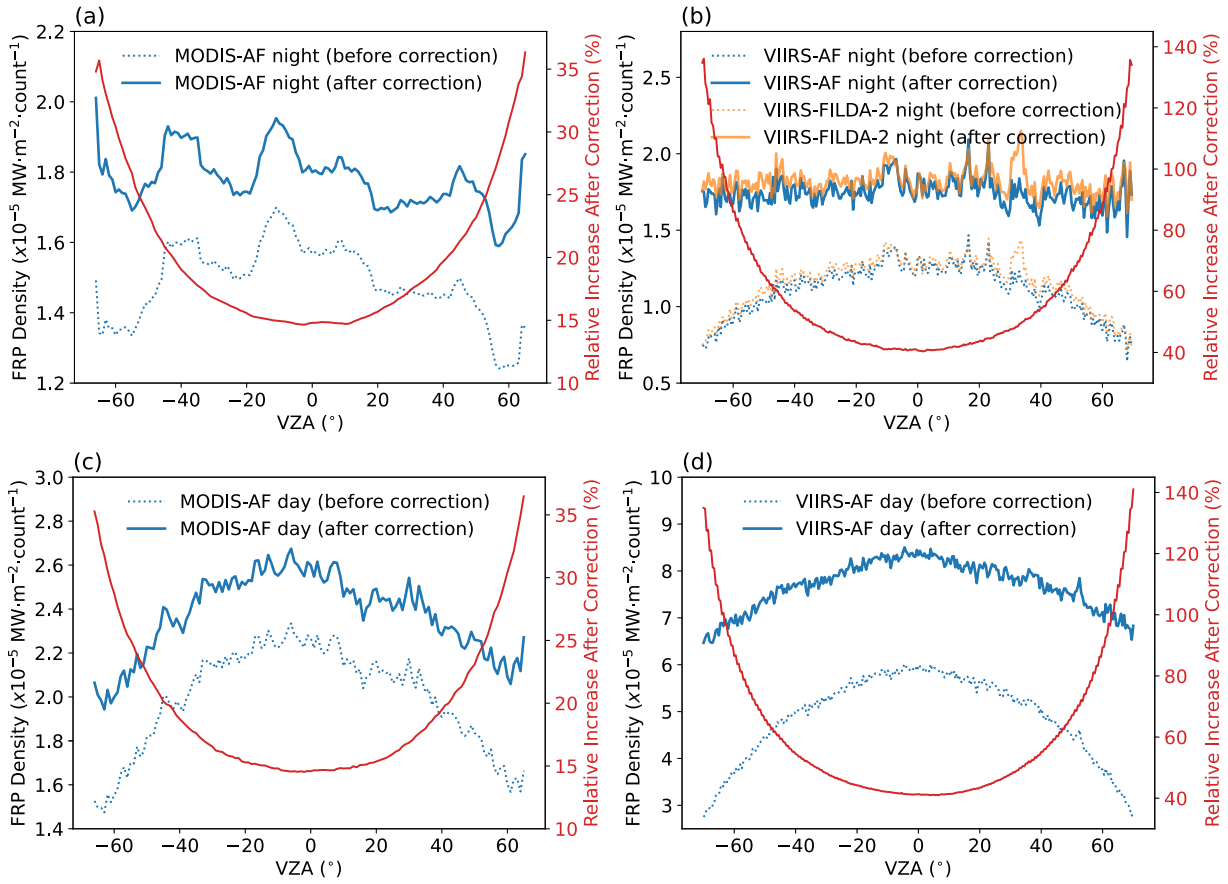

Fig. 8. (a) Angular dependency of the average FRP density before and after atmospheric correction for the nighttime MODIS AF product from June 2019 to May 2020. The red solid line is the relative increase after atmospheric correction. (b) Similar to (a), but for the nighttime VIIRS AF product (blue lines) and the nighttime VIIRS FILDA-2 product (orange lines). The red solid line is the relative increase after atmospheric correction for the nighttime VIIRS AF product. (c) Similar to (a), but for the daytime MODIS AF product. (d) Similar to (a), but for the daytime VIIRS AF product.

mitigate the artifacts of the angular dependency of global FRP retrieval. The atmosphere is assumed to be cloud-free as a rigid cloud mask is employed in the fire detection algorithms before FRP retrieval [28], [38], [51]. The surface is assumed to be a flat Lambertian surface, which could lead to uncertainties if subpixel fires are obscured by surrounding elevated terrain at larger VZAs [61], [62]. The gas vertical profile of the mid-latitude summer atmosphere is used. Sensitivity tests using different vertical shapes were conducted, and the transmittance difference was less than 1%. This indicates that the impacts of vertical shape on total gas absorption are marginal, while the total amount of gases may play a more important role. Finally, surface pressure is varied in the model, which is an indicator of total amount of gases in the path of radiative transfer, proportional to total gas absorption. As the relationship between the number of gas molecules and pressure (at a given temperature) is well described by the ideal gas law, the look-up tables of atmospheric transmittance below are only shown as a function of VZA and PW at sea level pressure.

B. Look-Up Table of Atmospheric Transmittance

The line-by-line one-way atmospheric transmittance is computed at the MODIS MIR channel (band 22, 3.96 μm) and VIIRS MIR channel (M13, 4.05 μm) under varying VZAs and PW. The primary gas absorbents at MIR are N_2, CO_2, N_2O, and water vapor [Fig. 1(a)]. To obtain the average atmospheric transmittance, the gas absorption spectra are convolved with sensor RSR function. The results are shown in Fig. 7(a) and (b). In nadir, under dry conditions (PW = 10 mm), the atmospheric transmittance is ~0.89 for MODIS and ~0.72 for VIIRS. However, off-nadir (VZA = 60°) with the same water vapor content, the atmospheric transmittance drops significantly to ~0.80 for MODIS and ~0.55 for VIIRS, marking a reduction in transmittance of 9% and 17%, respectively. This decrease in transmittance is attributed to the increased length of the light path, which amplifies total gas absorption. Furthermore, as water vapor content rises, the gas absorption from water vapor is also enhanced, leading to a decrease in atmospheric transmittance. For instance, in nadir, under wet conditions (PW = 70 mm), the atmospheric transmittance declines to ~0.78 for MODIS and ~0.63 for VIIRS (a reduction of 11% and 9%, respectively) when compared to dry conditions. It is worth highlighting that the VIIRS MIR channel exhibits reduced transparency compared to MODIS due to enhanced absorption from N_2 and CO_2. Consequently, the VIIRS MIR transmittance is 17% lower than that of MODIS under dry conditions in nadir, with the difference escalating to 25% off-nadir (VZA = 60°). This emphasizes that the need for atmospheric correction is even more vital for VIIRS than MODIS at the MIR channel.

At the VIIRS TIR-short channel (M14, 8.55 μm), water vapor dominates the total gas absorption, accounting for 96.8% of the total gas optical depth, followed by N_2O (2.3%), O_3 (0.6%), and CH_4 (0.2%) [Fig. 1(b)]. Convolving the gas

absorption spectra with sensor RSR function, Fig. 7(c) shows the average transmittance at the VIIRS TIR-short channel. Under dry conditions (PW = 10 mm), the transmittance is ∼0.80 in nadir and drops to ∼0.70 off-nadir (VZA = 60°), which is a 10% decrease with VZA. Furthermore, the TIR-short transmittance drops drastically with PW, with a value of 0.80 in nadir under dry conditions (PW = 10 mm) and 0.27 under wet conditions (PW = 70 mm), marking a significant reduction of 53%. This underscores the crucial importance of correcting for water vapor absorption in the two-channel FRP retrieval application. To address this, the PW data from GEOS-FP is incorporated for atmospheric correction.

C. Impacts of Atmospheric Correction

In this section, the impacts of atmospheric correction will be illustrated using the single-channel (MIR) FRP retrieval as an example. The implications extend analogously to two-channel FRP retrieval, although the latter is more impacted by water vapor absorption. Single-channel FRP retrievals are obtained from the MODIS AF, VIIRS AF, and VIIRS FILDA-2 products. For each detected fire hotspot, the corresponding MIR transmittance is determined based on VZA and GEOS-FP PW using the look-up tables provided in Fig. 7(a) and (b). With the knowledge of MIR transmittance, the atmospherically corrected one-channel FRP is calculated using (4).

1) Reduced Angular Dependency Artifact: The results in Fig. 8(a) and (b) demonstrate that after atmospheric correction, the artifact of the angular dependency of one-channel FRP retrieval at nighttime is effectively mitigated, if not entirely eliminated, for the MODIS AF, VIIRS AF, and VIIRS FILDA-2 products. The angular dependency is quantified using the mean FRP density (in $\mathrm{MW{\cdot}m^{-2}{\cdot}count^{-1}}$), normalized by pixel area to account for increasing pixel size with VZA, and normalized by fire count to account for decreased sensor sensitivity to fires with increasing pixel size. At night, before correction, all three products exhibit a prominent angular dependency of FRP (in $\mathrm{MW{\cdot}m^{-2}{\cdot}count^{-1}}$), with the FRP nadir (VZA < 10°) to off-nadir (VZA > 60°) ratio of 1.24 for MODIS AF, 1.55 for VIIRS AF, and 1.51 for VIIRS FILDA-2. After correction, their nadir to off-nadir ratio decreases to 1.07, 1.05, and 1.03, respectively, highlighting the effective mitigation of the angular dependency artifacts. Note that the top 1% of the data (in terms of mean FRP density) are excluded to remove the noise from extreme fire events. Additionally, the 9° running average is applied to the nighttime MODIS AF product to enhance signals from its limited observation (only 7% of the MODIS AF detections are at night during the study period). It is worth emphasizing that, prior to atmospheric correction, VIIRS AF and VIIRS FILDA-2 show a more pronounced angular dependency in FRP compared to MODIS AF. This is due to the more significant gas absorption at the VIIRS MIR channel, which is further amplified with rising VZA.

During the day, a notable reduction in the FRP angular dependency is also observed. The FRP nadir to off-nadir ratio decreases from 1.45 to 1.25 for MODIS AF, and from 1.77 to 1.21 for VIIRS AF [Fig. 8(c) and (d)]. Despite the significant mitigation, a residual daytime FRP angular dependency persists after atmospheric correction, potentially linked to the inherent bias in the MODIS AF and VIIRS AF algorithm for daytime fire detection. Taking the VIIRS I-band AF product as an example, the ratio of mean FRP density for the detected fire pixels between nadir and off-nadir is 1.77 during the day. For reference, this ratio is only 1.55 at night, which is the extent that can be accounted for by atmospheric correction in the FRP calculation [Fig. 8(b) and (d)]. The additional 22% in daytime angular dependency unaccounted for is attributed to the bias in fire detection. In fact, there is a strong angular dependency in the contextual thresholds used for daytime fire detection.

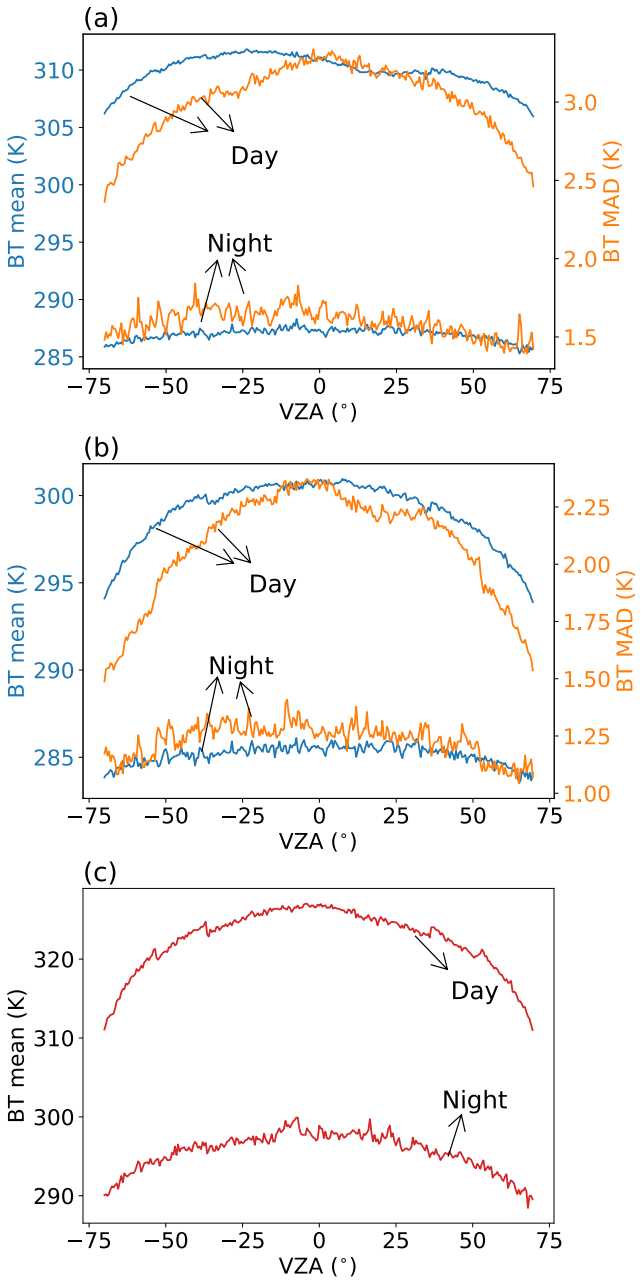

Fig. 9. Angular dependency (a) of the I4 (3.74 μm) BT mean (blue) and MAD (orange) of background pixels, (b) of the I5 (11.45 μm) BT mean (blue) and MAD (orange) of the background pixels, and (c) of the M13 (4.05 μm) BT of fire pixels, for the VIIRS AF product from June 2019 to May 2020.

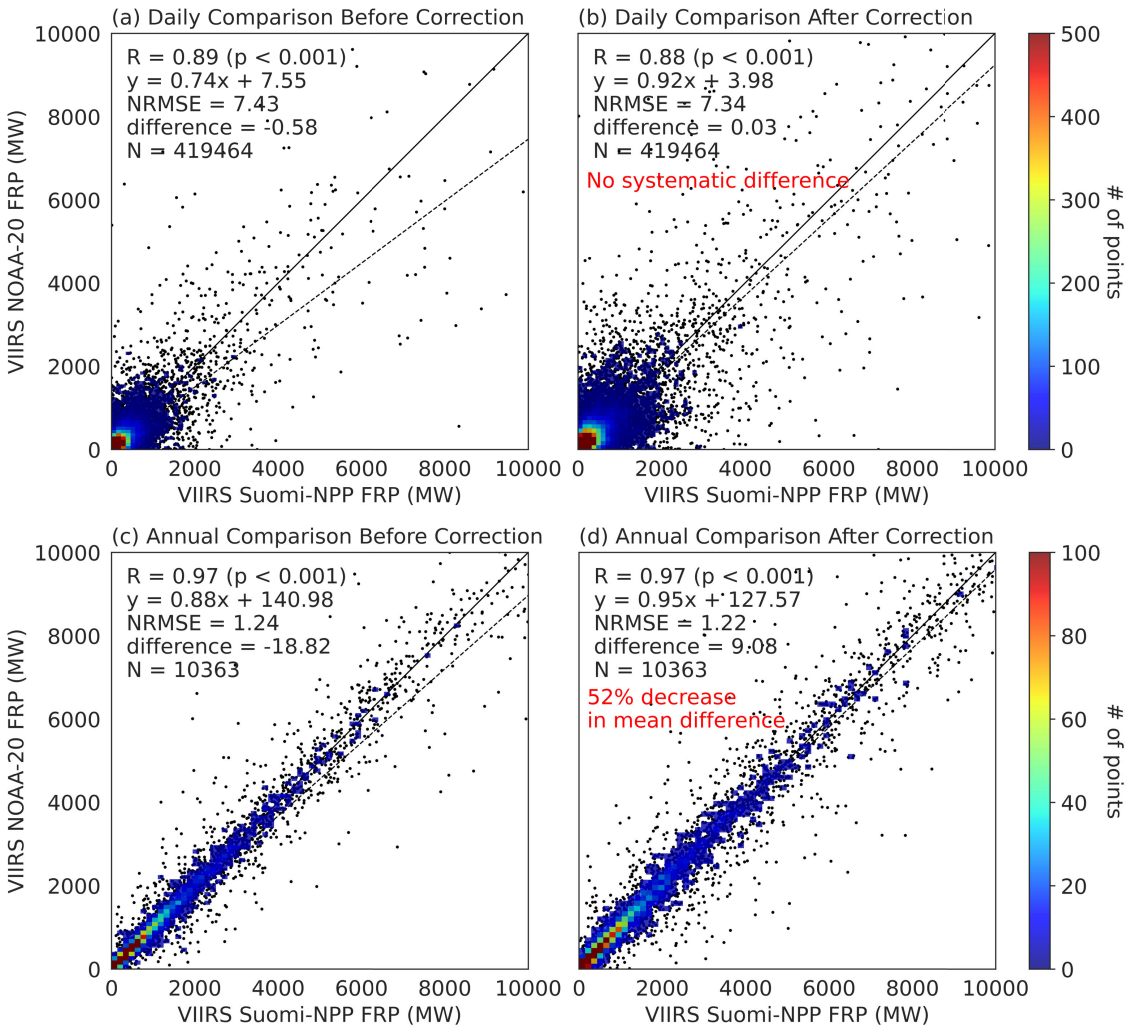

Fig. 10. Daily-by-day and grid-by-grid comparison of the nighttime VIIRS FILDA-2 one-channel FRP retrieval between Suomi-NPP and NOAA-20 (aggregated to 1° × 1° CMG) from June 2019 to May 2020 (a) before and (b) after atmospheric correction. The black solid line is the 1:1 line, the black dashed line is the best-fit line, and the color indicates the density of the data. (c) and (d) Similar to (a) and (b), but on an annual scale.

The contextual thresholds are determined based on the mean and the mean absolute deviation (MAD) of the I4 (3.74 μm) and I5 (11.45 μm) background pixel BT [51]. Nonetheless, during daytime, the mean and MAD of the I4 background pixel BT are higher in-nadir than off-nadir, with a nadir and off-nadir difference of 3.4 and 0.7 K, respectively, whereas the difference is much smaller at night (1.3 and 0.2 K, respectively) [Fig. 9(a)]. A similar day-night contrast is observed in the mean and MAD of the I5 background pixel BT, with a nadir and off-nadir difference of 5.0 and 0.7 K at day, and 1.3 and 0.2 K at night [Fig. 9(b)]. Hence, using these criteria which are themselves dependent on VZAs, the detected fire pixels in turn exhibit a more pronounced angular dependency of the M13 (4.05 μm) BT during the day. The fire pixel M13 BT has a nadir and off-nadir difference of 11.4 K during the day, while this difference is only 6.7 K at night [Fig. 9(c)]. In other words, fire pixels with a lower MIR BT/radiance can be detected off-nadir, due to the contextual test threshold being less stringent. This threshold, however, is in terms of the radiance of the entire fire pixel (composed of a fire component and a background component). The lower threshold off-nadir is orthogonal to, and should not be confused with decreased sensor sensitivity to the fire component off-nadir as pixel area grows (and fire fraction decreases), which leads to smaller and cooler fires being missed.

To further alleviate the daytime FRP angular dependency, it is essential to address the angular dependency of the thresholds used in the contextual test. For VIIRS, the angular dependency of the mean and MAD of the I4 (3.74 μm) and I5 (11.45 μm) background pixel radiance should be mitigated. One reason for the angular dependency of the above terms is possibly that, the background pixels which are supposed to be fire-free are actually not "clean" (i.e., there are fire signals in the background pixels), particularly in nadir. Expanding the window size for the contextual test is necessary for accurate characterization of the background I4 and I5 radiance. Currently, the window size is set to a minimum of 11 × 11 pixels (which can grow up to 31 × 31 pixels) for both nadir and off-nadir. In terms of area (unit: m^2), however, the window size is actually smaller in-nadir compared to off-nadir due to the increase of pixel size with VZA. This may potentially lead to less accurate background characterization in nadir (i.e.,

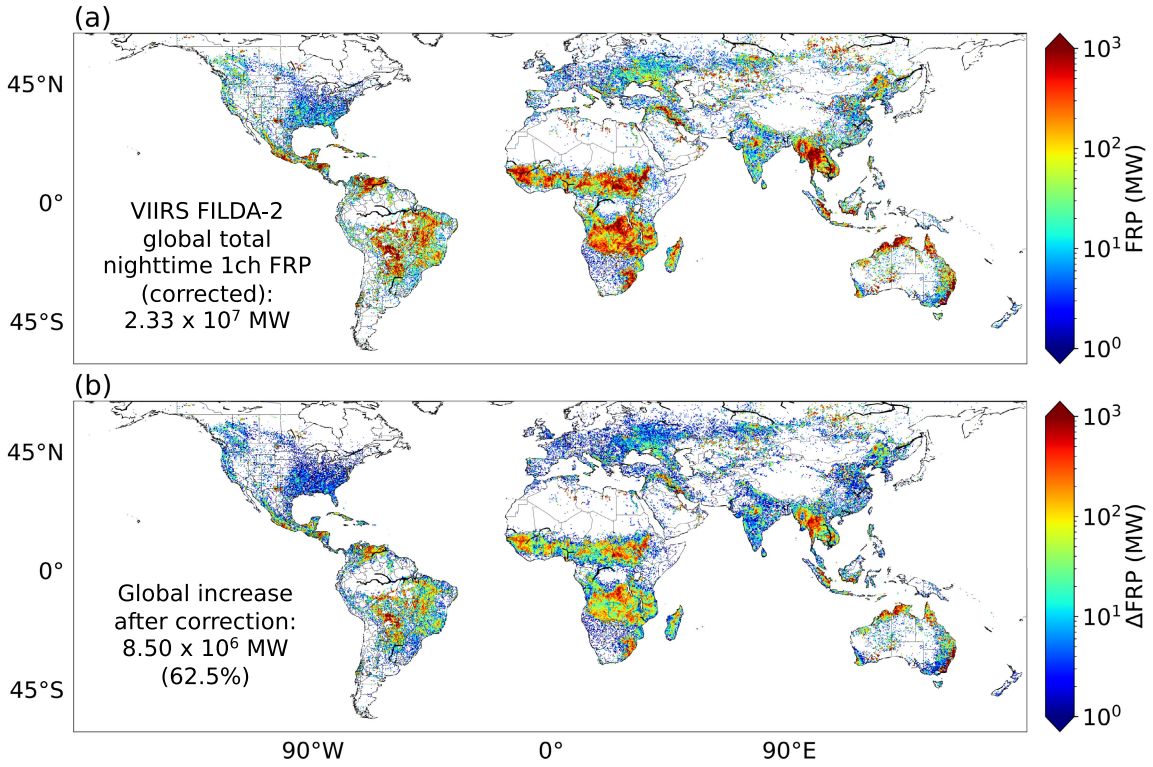

Fig. 11. (a) Global distribution of the nighttime VIIRS FILDA-2 atmospheric-corrected one-channel (MIR) FRP retrieval (aggregated to 0.25° × 0.25° CMG) from June 2019 to May 2020 and (b) its increase compared to the uncorrected FRP.

a higher mean I4 and I5 radiance of the background pixels from fire contamination, usually accompanied by a higher MAD of the I4 and I5 radiance due to surface temperature inhomogeneity). It is thereby desirable to use an enlarged window that is sufficient to minimize fire contamination, and one that varies with VZA (in terms of pixel number) to account for the pixel size difference and ensure equal area. The issue of the persisting daytime FRP angular dependency even after atmospheric correction is associated with the inherent bias in the daytime fire detection algorithm, which is a separate issue from FRP retrieval and will be addressed in a companion paper describing the daytime VIIRS FILDA-2 fire detection algorithm.

2) Improved Agreement Between VIIRS FILDA-2 for Suomi-NPP and NOAA-20: During the study period (June 2019–May 2020), Suomi-NPP flies half an orbit (approximately 50 min) ahead of NOAA-20. Despite this observation time difference, it is assumed that there are no significant differences in fire energy on a global and annual scale. Hence, the discrepancies between the VIIRS FILDA-2 Suomi-NPP and NOAA-20 FRP retrievals mainly stem from the differences in their viewing geometry (and hence different atmospheric attenuation in the MIR radiance), and can thereby be mitigated by atmospheric correction. To accommodate the observation footprint differences, the VIIRS FILDA-2 FRP retrievals from Suomi-NPP are NOAA-20 are aggregated to 1° × 1° CMG and compared grid-by-grid. The results, given in Fig. 10, demonstrate an improved agreement of nighttime one-channel VIIRS FILDA-2 FRP retrievals between Suomi-NPP and NOAA-20 post-correction. Their day-to-day comparison before correction exhibits an absolute mean difference of 0.58 MW, while there are almost no systematic differences (absolute mean difference = 0.03 MW) after correction. On an annual basis, the absolute mean difference decreases by 51.8% (from 18.82 to 9.08 MW) and the normalized RMSE decreases by 1.6% (from 1.24 to 1.22 MW). This suggests that atmospheric correction is effective in aligning the VIIRS FILDA-2 FRP retrievals for Suomi-NPP and NOAA-20, by reconciling the differences in atmospheric absorption at the MIR channel due to different viewing geometry.

3) Ubiquitous FRP Increase: Atmospheric correction leads to a ubiquitous FRP increase for all three fire products. For the MODIS AF product, there is a ∼15% increase in FRP in-nadir and ∼36% off-nadir (Fig. 8). The increase in FRP is approximately three times more significant for the VIIRS AF and VIIRS FILDA-2 products, with a ∼42% increase in nadir and a ∼140% increase off-nadir. This is due to correcting for the stronger gas absorption at the VIIRS MIR channel, which is 17% more significant than MODIS in-nadir and 25% off-nadir. Globally, from June 2019 to May 2020, there is a relative FRP increase of 20.8%, 65.8%, and 62.5%, respectively, for the MODIS AF product (including both daytime and nighttime) (Fig. S7), the VIIRS AF product (daytime and nighttime) (Fig. S8), and the VIIRS FILDA-2 product (nighttime only) (Fig. 11).

VI. Conclusion

The FRP retrievals from MODIS and VIIRS serve as the cornerstone for major global top-down fire emission inventories extensively used by the air pollution modeling community. This work contributes to constraining the FRP retrieval uncertainties from two perspectives. First, a novel two-channel FRP retrieval formula is proposed for VIIRS, by integrating the TIR-short (8.55 μm) channel alongside the conventional MIR

(4.05 μm) channel. This formulation, in theory, surpasses the traditional one-channel retrieval approach that solely relies on MIR with a 62% reduction in negative mean bias. The TIR-short channel adds to the FRP retrieval in its increased sensitivity to smoldering fires compared to the MIR channel, while in the meantime is less contaminated by non-fire background compared to the TIR ($\sim$11 μm) channel employed by previous studies using the bispectral approach. Applying the two-channel FRP retrieval method on the VIIRS FILDA-2 product yields results that are consistent with those obtained from the Monte Carlo simulation.

Second, atmospheric correction is performed on the MODIS MIR, VIIRS MIR, and VIIRS TIR-short channels given the significant atmospheric absorption. N_2 dominates absorption for MODIS MIR, CO_2 for VIIRS MIR, and water vapor for VIIRS TIR-short. In nadir, atmospheric transmittance is 0.89 for MODIS MIR, 0.72 for VIIRS MIR, and 0.80 for VIIRS TIR-short. The transmittance decreases with increasing VZA (0.80 for MODIS MIR, 0.55 for VIIRS MIR, and 0.70 for VIIRS TIR-short at VZA = 60°). Notably, the VIIRS MIR channel is less transparent than MODIS MIR (17% less in-nadir and 25% off-nadir) due to enhanced absorption from N_2 and CO_2, highlighting the even greater importance of atmospheric correction for VIIRS. In addition, the VIIRS TIR-short channel is heavily impacted by water vapor absorption, with transmittance decreased by 53% as PW increases from 10 to 70 mm. This underscores the importance of considering variations in water vapor content, especially in the application of two-channel FRP retrieval.

Furthermore, the significance of atmospheric correction is demonstrated from three aspects using the one-channel FRP retrievals from the MODIS AF product, VIIRS AF product, and VIIRS FILDA-2 product. The significance is also indicative for two-channel FRP retrieval. First, the artifact of FRP angular dependency due to increased atmospheric attenuation with VZA is effectively reduced after atmospheric correction. The FRP nadir to off-nadir ratio decreases from 1.24 (1.45) to 1.07 (1.25) for nighttime (daytime) MODIS AF, from 1.55 (1.77) to 1.05 (1.21) for nighttime (daytime) VIIRS AF, and from 1.51 to 1.03 for nighttime VIIRS FILDA-2. While the FRP angular dependency is nearly eliminated at night, there is a residual daytime angular dependency even after correction. This is because the thresholds used in the contextual test are strongly dependent on VZA in the daytime fire detection algorithm, resulting in an inherent bias in the fires detected that cannot be accounted for by conducting atmospheric correction in the FRP calculation. Second, an enhanced consistency is observed between the VIIRS FILDA-2 Suomi-NPP FRP retrieval and NOAA-20 FRP retrieval, attributed to atmospheric correction reconciling the differences in the atmospheric absorption at the MIR channels due to different viewing geometry. Third, there is an omnipresent FRP increase for all three products, with VIIRS experiencing a more substantial rise than MODIS. The MODIS AF product shows approximately 15% and 36% increases in-nadir and off-nadir, respectively. In contrast, the VIIRS AF and VIIRS FILDA-2 products demonstrate more significant increases due to correcting for stronger gas absorption at the VIIRS MIR channel, reaching 42% in-nadir and 140% off-nadir. Globally and annually (June 2019–May 2020), the relative FRP increases are 20.8%, 65.8%, and 62.5% for the MODIS AF product, VIIRS AF product, and VIIRS FILDA-2 product, respectively.

VII. Implications and Outlooks

The improvements in the MODIS and VIIRS FRP retrievals have several implications for the downstream top-down fire emission inventory products. Currently, many such inventories depend on a scaling factor to ensure that the modeled aerosol optical depth (AOD) aligns with observed AOD climatologically on a global/regional scale [6], [7], [8]. While a climatological scaling factor maintains overall consistency with observation when averaged spatiotemporally, its application to individual fires may result in overestimation or underestimation, depending on the accuracy of the FRP retrieval for each specific fire. Although some studies employ VZA-dependent scaling factors and found better agreement between MODIS and VIIRS FRP, their approach remains empirical and does not consider the underlying physical processes (e.g., atmospheric absorption) that influence the accuracy of FRP retrieval at various VZAs [48]. This study addresses the gap with a focus on the inherent physical processes (such as fire combustion efficiency and atmospheric correction) and aims to enhance the FRP retrieval accuracy for each individual fire, which, in turn, holds the potential for an overall improvement when translated into fire emissions. Specifically, the mitigation of the angular dependency artifact of FRP through atmospheric correction signifies a parallel improvement in the resulting fire emissions. This improvement directly addresses the fluctuations induced by day-to-day changes in satellite orbit, ensuring improved dynamics in fire emissions. Furthermore, the enhanced agreement of the VIIRS FILDA-2 FRP retrievals between VIIRS Suomi-NPP and NOAA-20 implies a more consistent depiction of fire emissions derived from different platforms. With the decommission of MODIS, a better continuity is implied as major fire emission inventories transition to VIIRS.

Acknowledgment

The authors acknowledge the public availability of the Visible Infrared Imaging Radiometer Suite (VIIRS) and Moderate Resolution Imaging Spectroradiometer (MODIS) data from the Earth Observing System Data and Information System (EOSDIS) at the National Aeronautics and Space Administration (NASA). They would like to thank NASA Global Modeling and Assimilation Office (GMAO) for the public availability of the Goddard Earth Observing System Forward Processing (GEOS-FP) data.

References

[1] J. Wang, Y. Yue, Y. Wang, C. Ichoku, L. Ellison, and J. Zeng, "Mitigating satellite-based fire sampling limitations in deriving biomass burning emission rates: Application to WRF-chem model over the northern sub-Saharan African region," *J. Geophys. Res., Atmos.*, vol. 123, no. 1, pp. 507–528, Jan. 2018, doi: 10.1002/2017jd026840.

[2] R. Aguilera, T. Corringham, A. Gershunov, and T. Benmarhnia, "Wildfire smoke impacts respiratory health more than fine particles from other sources: Observational evidence from southern California," *Nature Commun.*, vol. 12, no. 1, p. 1493, Mar. 2021, doi: 10.1038/s41467-021-21708-0.

[3] P. J. Crutzen and M. O. Andreae, "Biomass burning in the tropics: Impact on atmospheric chemistry and biogeochemical cycles," *Science*, vol. 250, no. 4988, pp. 1669–1678, Dec. 1990, doi: 10.1126/science.250.4988.1669.

[4] W. Deng, J. B. Cohen, S. Wang, and C. Lin, "Improving the understanding between climate variability and observed extremes of global NO_2 over the past 15 years," *Environ. Res. Lett.*, vol. 16, no. 5, May 2021, Art. no. 054020, doi: 10.1088/1748-9326/abd502.

[5] Y. Ming, V. Ramaswamy, and G. Persad, "Two opposing effects of absorbing aerosols on global-mean precipitation," *Geophys. Res. Lett.*, vol. 37, 2010, Art. no. L13701, doi: 10.1029/2010gl042895.

[6] A. S. Darmenov and A. da Silva. (2015). *The Quick Fire Emissions Dataset (QFED)—Documentation of Versions 2.1, 2.2 and 2.4*. NASA Global Model. Assimilation Office. [Online]. Available: https://gmao.gsfc.nasa.gov/pubs/docs/Darmenov796.pdf

[7] C. Ichoku and L. Ellison, "Global top-down smoke-aerosol emissions estimation using satellite fire radiative power measurements," *Atmos. Chem. Phys.*, vol. 14, no. 13, pp. 6643–6667, Jul. 2014. [Online]. Available: https://acp.copernicus.org/articles/14/6643/2014/

[8] J. W. Kaiser et al., "Biomass burning emissions estimated with a global fire assimilation system based on observed fire radiative power," *Biogeosciences*, vol. 9, no. 1, pp. 527–554, Jan. 2012. [Online]. Available: https://bg.copernicus.org/articles/9/527/2012/

[9] M. J. Wooster, G. Roberts, G. L. W. Perry, and Y. J. Kaufman, "Retrieval of biomass combustion rates and totals from fire radiative power observations: FRP derivation and calibration relationships between biomass consumption and fire radiative energy release," *J. Geophys. Res., Atmos.*, vol. 110, 2005, Art. no. D24311, doi: 10.1029/2005jd006318.

[10] W. Seiler and P. J. Crutzen, "Estimates of gross and net fluxes of carbon between the biosphere and the atmosphere from biomass burning," *Climatic Change*, vol. 2, no. 3, pp. 207–247, 1980, doi: 10.1007/bf00137988.

[11] G. R. van der Werf et al., "Global fire emissions and the contribution of deforestation, savanna, forest, agricultural, and peat fires (1997–2009)," *Atmos. Chem. Phys.*, vol. 10, no. 23, pp. 11707–11735, Dec. 2010. [Online]. Available: https://acp.copernicus.org/articles/10/11707/2010/

[12] C. Wiedinmyer et al., "The fire inventory from NCAR (FINN): A high resolution global model to estimate the emissions from open burning," *Geosci. Model Develop.*, vol. 4, no. 3, pp. 625–641, Jul. 2011. [Online]. Available: https://gmd.copernicus.org/articles/4/625/2011/

[13] J. S. Reid, R. Koppmann, T. F. Eck, and D. P. Eleuterio, "A review of biomass burning emissions Part II: Intensive physical properties of biomass burning particles," *Atmos. Chem. Phys.*, vol. 5, no. 3, pp. 799–825, Mar. 2005. [Online]. Available: https://acp.copernicus.org/articles/5/799/2005/

[14] J. S. Reid et al., "Global monitoring and forecasting of biomass-burning smoke: Description of and lessons from the fire locating and modeling of burning emissions (FLAMBE) program," *IEEE J. Sel. Topics Appl. Earth Observ. Remote Sens.*, vol. 2, no. 3, pp. 144–162, Sep. 2009.

[15] G. A. Ferrada et al., "Introducing the VIIRS-based fire emission inventory version 0 (VFEIv0)," *Geosci. Model Develop.*, vol. 15, no. 21, pp. 8085–8109, Nov. 2022. [Online]. Available: https://gmd.copernicus.org/articles/15/8085/2022/

[16] X. Pan et al., "Six global biomass burning emission datasets: Intercomparison and application in one global aerosol model," *Atmos. Chem. Phys.*, vol. 20, no. 2, pp. 969–994, Jan. 2020. [Online]. Available: https://acp.copernicus.org/articles/20/969/2020/

[17] F. Zhang et al., "Sensitivity of mesoscale modeling of smoke direct radiative effect to the emission inventory: A case study in northern sub-Saharan African region," *Environ. Res. Lett.*, vol. 9, no. 7, Jul. 2014, Art. no. 075002, doi: 10.1088/1748-9326/9/7/075002.

[18] T. Liu et al., "Diagnosing spatial biases and uncertainties in global fire emissions inventories: Indonesia as regional case study," *Remote Sens. Environ.*, vol. 237, Feb. 2020, Art. no. 111557. [Online]. Available: https://www.sciencedirect.com/science/article/pii/S0034425719305772

[19] M. O. Andreae, "Emission of trace gases and aerosols from biomass burning—An updated assessment," *Atmos. Chem. Phys.*, vol. 19, no. 13, pp. 8523–8546, Jul. 2019. [Online]. Available: https://acp.copernicus.org/articles/19/8523/2019/

[20] J. B. Cohen, "Quantifying the occurrence and magnitude of the southeast Asian fire climatology," *Environ. Res. Lett.*, vol. 9, no. 11, Nov. 2014, Art. no. 114018, doi: 10.1088/1748-9326/9/11/114018.

[21] C. Ge, J. Wang, J. S. Reid, D. J. Posselt, P. Xian, and E. Hyer, "Mesoscale modeling of smoke transport from equatorial southeast Asian maritime continent to the philippines: First comparison of ensemble analysis with in situ observations," *J. Geophys. Research: Atmos.*, vol. 122, no. 10, pp. 5380–5398, May 2017, doi: 10.1002/2016jd026241.

[22] C. Lin, J. B. Cohen, S. Wang, R. Lan, and W. Deng, "A new perspective on the spatial, temporal, and vertical distribution of biomass burning: Quantifying a significant increase in CO emissions," *Environ. Res. Lett.*, vol. 15, no. 10, Oct. 2020, Art. no. 104091, doi: 10.1088/1748-9326/abaa7a.

[23] P. E. Saide et al., "Revealing important nocturnal and day-to-day variations in fire smoke emissions through a multiplatform inversion," *Geophys. Res. Lett.*, vol. 42, no. 9, pp. 3609–3618, May 2015, doi: 10.1002/2015gl063737.

[24] J. Wang et al., "Mesoscale modeling of central American smoke transport to the United States: 1. 'Top-down' assessment of emission strength and diurnal variation impacts," *J. Geophys. Res., Atmos.*, vol. 111, 2006, Art. no. D05S17, doi: 10.1029/2005jd006416.

[25] J. Wang et al., "Mesoscale modeling of smoke transport over the southeast Asian Maritime continent: Interplay of sea breeze, trade wind, typhoon, and topography," *Atmos. Res.*, vol. 122, pp. 486–503, Mar. 2013. [Online]. Available: https://www.sciencedirect.com/science/article/pii/S016980951200138X

[26] S. Wang, J. B. Cohen, W. Deng, K. Qin, and J. Guo, "Using a new top-down constrained emissions inventory to attribute the previously unknown source of extreme aerosol loadings observed annually in the monsoon Asia free troposphere," *Earth's Future*, vol. 9, no. 7, Jul. 2021, Art. no. e2021EF002167, doi: 10.1029/2021ef002167.

[27] S. Wang, J. B. Cohen, C. Lin, and W. Deng, "Constraining the relationships between aerosol height, aerosol optical depth and total column trace gas measurements using remote sensing and models," *Atmos. Chem. Phys.*, vol. 20, no. 23, pp. 15401–15426, 2020, doi: 10.5194/acp-20-15401-2020. [Online]. Available: https://acp.copernicus.org/articles/20/15401/2020/

[28] L. Giglio, W. Schroeder, and C. O. Justice, "The collection 6 MODIS active fire detection algorithm and fire products," *Remote Sens. Environ.*, vol. 178, pp. 31–41, Jun. 2016. [Online]. Available: https://www.sciencedirect.com/science/article/pii/S0034425716300827

[29] W. Xu, M. J. Wooster, G. Roberts, and P. Freeborn, "New GOES imager algorithms for cloud and active fire detection and fire radiative power assessment across North, South and Central America," *Remote Sens. Environ.*, vol. 114, no. 9, pp. 1876–1895, 2010, doi: 10.1016/j.rse.2010.03.012. [Online]. Available: https://www.sciencedirect.com/science/article/pii/S0034425710001094

[30] T. N. Polivka, J. Wang, L. T. Ellison, E. J. Hyer, and C. M. Ichoku, "Improving nocturnal fire detection with the VIIRS day–night band," *IEEE Trans. Geosci. Remote Sens.*, vol. 54, no. 9, pp. 5503–5519, Sep. 2016.

[31] J. Wang et al., "Detecting nighttime fire combustion phase by hybrid application of visible and infrared radiation from Suomi NPP VIIRS," *Remote Sens. Environ.*, vol. 237, Feb. 2020, Art. no. 111466. [Online]. Available: https://www.sciencedirect.com/science/article/pii/S0034425719304857

[32] P. Kaaret et al., "On the potential of hotspot detection at night via multiband visible/near-infrared imaging," *Remote Sens.*, vol. 14, no. 19, p. 5019, 2022.

[33] M. Zhou et al., "Nighttime smoke aerosol optical depth over US rural areas: First retrieval from VIIRS moonlight observations," *Remote Sens. Environ.*, vol. 267, 2021, Art. no. 112717.

[34] M. Zhou et al., "First lunar-light mapping of nighttime dust season oceanic aerosol optical depth over North Atlantic from space," *Remote Sens. Environ.*, vol. 312, 2024, Art. no. 114315.

[35] J. Song et al., "Characterization of urban heat islands using city lights: Insights from MODIS and VIIRS DNB observations," *Remote Sens.*, vol. 13, no. 16, p. 3180, 2021.

[36] Q. Xiao et al., "County-level artificial light at night (ALAN) in the contiguous US (2012–2019): Spatial variations, temporal trends, and environmental justice analyses," *Environ. Sci. Pollut. Res.*, vol. 30, no. 54, pp. 115870–115881, 2023.

[37] Q. Xiao et al., "Artificial light at night and social vulnerability: An environmental justice analysis in the US 2012–2019," *Environ. Int.*, vol. 178, 2023, Art. no. 108096.

[38] M. Zhou et al., "Enhancement of nighttime fire detection and combustion efficiency characterization using suomi-NPP and NOAA-20 VIIRS instruments," *IEEE Trans. Geosci. Remote Sens.*, vol. 61, 2023, Art. no. 4402420.

[39] M. Wooster, "Fire radiative energy for quantitative study of biomass burning: Derivation from the BIRD experimental satellite and comparison to MODIS fire products," *Remote Sens. Environ.*, vol. 86, no. 1, pp. 83–107, Jun. 2003. [Online]. Available: https://www.sciencedirect.com/science/article/pii/S0034425703000701

[40] J. Dozier, "A method for satellite identification of surface temperature fields of subpixel resolution," *Remote Sens. Environ.*, vol. 11, pp. 221–229, Jan. 1981. [Online]. Available: https://www.sciencedirect.com/science/article/pii/0034425781900213

[41] B. Zhukov, E. Lorenz, D. Oertel, M. Wooster, and G. Roberts, "Spaceborne detection and characterization of fires during the bi-spectral infrared detection (BIRD) experimental small satellite mission (2001–2004)," *Remote Sens. Environ.*, vol. 100, no. 1, pp. 29–51, Jan. 2006. [Online]. Available: https://www.sciencedirect.com/science/article/pii/S0034425705003123

[42] D. Peterson, J. Wang, C. Ichoku, E. Hyer, and V. Ambrosia, "A sub-pixel-based calculation of fire radiative power from MODIS observations: 1: Algorithm development and initial assessment," *Remote Sens. Environ.*, vol. 129, pp. 262–279, Apr. 2013. [Online]. Available: https://www.sciencedirect.com/science/article/pii/S0034425712004300

[43] L. Giglio and W. Schroeder, "A global feasibility assessment of the bi-spectral fire temperature and area retrieval using MODIS data," *Remote Sens. Environ.*, vol. 152, pp. 166–173, Sep. 2014. [Online]. Available: https://www.sciencedirect.com/science/article/pii/S0034425714002235

[44] D. Peterson and J. Wang, "A sub-pixel-based calculation of fire radiative power from MODIS observations: 2. Sensitivity analysis and potential fire weather application," *Remote Sens. Environ.*, vol. 129, pp. 231–249, Feb. 2013. [Online]. Available: https://www.sciencedirect.com/science/article/pii/S0034425712004087

[45] L. Giglio et al., "Active fire detection and characterization with the Advanced Spaceborne Thermal Emission and Reflection Radiometer (ASTER)," *Remote Sens. Environ.*, vol. 112, no. 6, pp. 3055–3063, Jun. 2008. [Online]. Available: https://www.sciencedirect.com/science/article/pii/S0034425708000825

[46] Y. J. Kaufman et al., "Potential global fire monitoring from EOS-MODIS," *J. Geophys. Res., Atmos.*, vol. 103, no. D24, pp. 32215–32238, Dec. 1998, doi: 10.1029/98jd01644.

[47] K. E. Trenberth, J. Fasullo, and L. Smith, "Trends and variability in column-integrated atmospheric water vapor," *Climate Dyn.*, vol. 24, nos. 7–8, pp. 741–758, Jun. 2005, doi: 10.1007/s00382-005-0017-4.

[48] I. Kaur, I. Hüser, T. Zhang, B. Gehrke, and J. Kaiser, "Correcting swath-dependent bias of MODIS FRP observations with quantile mapping," *Remote Sens.*, vol. 11, no. 10, p. 1205, May 2019. [Online]. Available: https://www.mdpi.com/2072-4292/11/10/1205

[49] F. Li, X. Zhang, S. Kondragunta, and I. Csiszar, "Comparison of fire radiative power estimates from VIIRS and MODIS observations," *J. Geophys. Res., Atmos.*, vol. 123, no. 9, pp. 4545–4563, May 2018, doi: 10.1029/2017jd027823.

[50] D. Fisher and M. J. Wooster, "Shortwave IR adaption of the mid-infrared radiance method of fire radiative power (FRP) retrieval for assessing industrial gas flaring output," *Remote Sens.*, vol. 10, no. 2, p. 305, Feb. 2018. [Online]. Available: https://www.mdpi.com/2072-4292/10/2/305

[51] W. Schroeder, P. Oliva, L. Giglio, and I. A. Csiszar, "The new VIIRS 375 m active fire detection data product: Algorithm description and initial assessment," *Remote Sens. Environ.*, vol. 143, pp. 85–96, Mar. 2014. [Online]. Available: https://www.sciencedirect.com/science/article/pii/S0034425713004483

[52] D. Peterson, E. Hyer, and J. Wang, "Quantifying the potential for high-altitude smoke injection in the North American boreal forest using the standard MODIS fire products and subpixel-based methods," *J. Geophys. Res., Atmos.*, vol. 119, no. 6, pp. 3401–3419, Mar. 2014.

[53] L. Giglio, J. Descloitres, C. O. Justice, and Y. J. Kaufman, "An enhanced contextual fire detection algorithm for MODIS," *Remote Sens. Environ.*, vol. 87, nos. 2–3, pp. 273–282, Oct. 2003. [Online]. Available: https://www.sciencedirect.com/science/article/pii/S0034425703001846

[54] I. Csiszar et al., "Active fires from the suomi NPP Visible Infrared Imaging Radiometer Suite: Product status and first evaluation results," *J. Geophys. Res., Atmos.*, vol. 119, no. 2, pp. 803–816, Jan. 2014, doi: 10.1002/2013JD020453.

[55] M. M. Rienecker et al., "The GEOS-5 data assimilation system-documentation of versions 5.0.1, 5.1.0, and 5.2.0," NASA, Goddard Space Flight Center, Greenbelt, MD, USA, Tech. Rep. NASA/TM-2008-104606-VOL-27, 2008. [Online]. Available: https://ntrs.nasa.gov/citations/20120011955

[56] Nat. Aeronaut. Space Admin. (2014). *VIIRS Radiometric Calibration Algorithm Theoretical Basis Document (ATBD)*. [Online]. Available: https://ladsweb.modaps.eosdis.nasa.gov/api/v2/content/archives/Document%20Archive/Science%20Data%20Product%20Documentation/Product%20Generation%20Algorithms/NASARevisedJPSSVIIRSRadCalATBD2014.pdf

[57] J. Wang et al., "A numerical testbed for remote sensing of aerosols, and its demonstration for evaluating retrieval synergy from a geostationary satellite constellation of GEO-CAPE and GOES-R," *J. Quant. Spectrosc. Radiat. Transf.*, vol. 146, pp. 510–528, Oct. 2014. [Online]. Available: https://www.sciencedirect.com/science/article/pii/S0022407314001368

[58] J. Wang et al., "Development of a nighttime shortwave radiative transfer model for remote sensing of nocturnal aerosols and fires from VIIRS," *Remote Sens. Environ.*, vol. 241, May 2020, Art. no. 111727. [Online]. Available: https://www.sciencedirect.com/science/article/pii/S0034425720300973

[59] AMS. (2024). *Glossary of Meteorology*. [Online]. Available: https://glossary.ametsoc.org/wiki/Precipitable_water

[60] A. P. Ferreira and L. Gimeno, "Determining precipitable water vapour from upper-air temperature, pressure and geopotential height," *Quart. J. Roy. Meteorolog. Soc.*, vol. 150, no. 758, pp. 484–522, Jan. 2024, doi: 10.1002/qj.4609.

[61] Z.-W. He and B.-H. Tang, "Retrieval of rugged mountainous areas Land Surface Temperature from high-spatial-resolution thermal infrared remote sensing data," *IEEE Trans. Geosci. Remote Sens.*, vol. 61, 2023, Art. no. 4508216.

[62] G. Yan, Z.-H. Jiao, T. Wang, and X. Mu, "Modeling surface longwave radiation over high-relief terrain," *Remote Sens. Environ.*, vol. 237, Feb. 2020, Art. no. 111556. [Online]. Available: https://www.sciencedirect.com/science/article/pii/S0034425719305760